

NOISE-ADAPTIVE DIFFUSION SAMPLING FOR INVERSE PROBLEMS WITHOUT TASK-SPECIFIC TUNING

Setthakorn Tanomkiattikun^{1,3} Zaiwang Gu² Liangli Zhen¹ Yingzhi Xia^{1 *}

¹Institute of High Performance Computing, Agency for Science, Technology and Research, Singapore

²Institute for Infocomm Research, Agency for Science, Technology and Research, Singapore

³Johns Hopkins University

stanomk1@jhu.edu {Gu_Zaiwang, zhen_liangli, Xia_Yingzhi}@a-star.edu.sg

ABSTRACT

Diffusion models (DMs) have recently shown remarkable performance on inverse problems (IPs). Optimization-based methods can fast solve IPs using DMs as powerful regularizers, but it is susceptible to local minima and noise overfitting. Although DMs can provide strong priors for Bayesian approaches, enforcing measurement consistency during the denoising process leads to manifold infeasibility issues. We propose Noise-space Hamiltonian Monte Carlo (N-HMC), a posterior sampling method that treats reverse diffusion as a deterministic mapping from initial noise to clean images. N-HMC enables comprehensive exploration of the solution space, avoiding local optima. By moving inference entirely into the initial-noise space, N-HMC keeps proposals on the learned data manifold. We provide a comprehensive theoretical analysis of our approach and extend the framework to a noise-adaptive variant (NA-NHMC) that effectively handles IPs with unknown noise type and level. Extensive experiments across four linear and three nonlinear inverse problems demonstrate that NA-NHMC achieves superior reconstruction quality with robust performance across different hyperparameters and initializations, significantly outperforming recent state-of-the-art methods. The code is available on <https://github.com/NA-HMC/NA-HMC>.

1 INTRODUCTION

Inverse problems (IPs) have wide applications in many domains, including computer vision (Janai et al., 2021; Quan et al., 2024), protein science (Yi et al., 2023; Ouyang-Zhang et al., 2023; Yang et al., 2019), medical imaging (Song et al., 2022b; Chu et al., 2025; Dao et al., 2024), scientific computing (Zheng et al., 2025; Xia & Zabaras, 2022; Xu et al., 2024). The goal is to reconstruct an unknown $\mathbf{x} \in \mathbb{R}^n$ from noisy measurements $\mathbf{y} \in \mathbb{R}^m$:

$$\mathbf{y} = \mathcal{A}(\mathbf{x}) + \eta, \quad (1)$$

where \mathcal{A} is a known forward operator, and $\eta \in \mathbb{R}^m$ is additive noise. Diffusion models (DMs) have recently shown powerful capabilities in modeling complex data distributions, which can provide a powerful class of priors for high-dimensional data x in solving IPs. Existing diffusion-based methods have demonstrated remarkable success across diverse inverse problems (Chung et al., 2023; Daras et al., 2024; Zheng et al., 2025; Song et al., 2022b).

Although remarkable progress has been made, as illustrated in Figure 1, current diffusion-based methods suffer from three complementary limitations and issues: (1) Iterative guidance methods such as DPS (Chung et al., 2023), DDRM (Kawar et al., 2022), DDNM (Wang et al., 2023), PIIGDM (Song et al., 2023), and TMPD (Boys et al., 2024) use the likelihood term to shift intermediate images directly, systematically pushing intermediate states off the learned data manifold and violating the training-time noise-conditioning of the denoiser, resulting in various failure reconstructions like like accumulated artifacts as shown in Figure 1 (a). (2) Stochastic MAP methods that optimize in image space, including ReSample (Song et al., 2024), DiffPIR (Zhu et al., 2023), DAPS (Zhang

* Corresponding author.

et al., 2024), SITCOM (Alkhouri et al., 2025a), and DIIP (Chihaoui & Favaro, 2025a) can match y well with very sharp details but require carefully tuned hyperparameters to not overfit to noise. This limits their effectiveness in high or unknown noise settings. (3) Deterministic MAP methods that optimize in the DM noise space (DMPlug, (Wang et al., 2024)) remove randomness but often get stuck in a single mode, especially in severely ill-posed problems like phase retrieval, due to a lack of posterior exploration. In short, enforcing data consistency mid-diffusion can break prior adherence, while optimizing only for fidelity leads to overfitting or mode collapse. Building a solution that maintains both measurement fidelity and manifold adherence remains open.

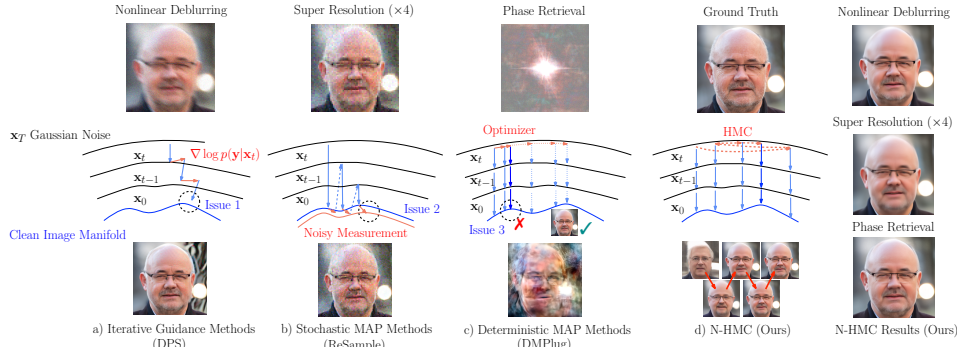


Figure 1: Comparison of existing methods and their limitations with the N-HMC method. (a) Iterative Guidance Methods (*DPS*) lead to *manifold infeasibility*. (b) Stochastic MAP methods (*Re-Sample*) (Song et al., 2024) are susceptible to *overfitting to noise*. (c) Deterministic MAP methods (*DMPlug*) (Wang et al., 2024) become *trapped in a local mode*. (d) Our method performs sampling in the noise space x_T and maps samples to images via a deterministic mapping $x_0 = \mathcal{D}(x_T)$.

Sampling from the full posterior ensures that the learned prior acts automatically as a regularizer, while an annealing schedule for noise standard deviation σ_y promotes efficient exploration and prevents the sampler from being trapped in early local modes. Importantly, the method relies only on a fixed set of hyperparameters that remain constant across tasks, datasets, levels of measurement noise, avoiding the repeated tuning required by many existing approaches.

To address the practical challenges that the measurement noise level is often unknown, we further introduce a Noise-Adaptive N-HMC (NA-NHMC). Instead of requiring a fixed noise level, we take a principled Bayesian approach, placing a non-informative prior on the noise variance and marginalizing it out. This yields a parameter-free likelihood term that automatically adapts to the true underlying noise in the measurements. As shown in experiments, this allows NA-NHMC to achieve robust, high-quality reconstructions across varying and even unknown noise types and levels without any task-specific hyperparameter tuning. In contrast, the performance of other methods depends on the hyperparameters listed in Section A.5, which were specifically tuned for Gaussian noise. Our key *contributions* include: (1) In Section 3.1, we propose N-HMC, a posterior sampling method that addresses the three key limitations of existing state-of-the-art (SOTA) approaches. We further analyze its sampling behavior and provide a theoretical guarantee of its robustness to measurement noise in Section 3.2 and Appendix A.2. (2) In Section 3.3, we extend our method to settings with unknown noise types and levels. We show that it outperforms SOTA methods on most metrics (Section 4.3), especially for non-linear and high noise problems. (3) In extensive experiments, NA-NHMC method solves diverse inverse problem tasks under unknown noise types and levels without any task- or noise-specific hyperparameter tuning, in contrast to many existing methods. (4) We demonstrate in Section 4.1 that the annealing schedule for σ_y helps promote early exploration and prevent local-mode collapse, especially in severely ill-posed tasks like phase retrieval.

2 PRELIMINARIES

2.1 DIFFUSION MODELS FOR INVERSE PROBLEMS

Daras et al. (2024) broadly classifies methods for solving inverse problems (IPs) into two categories. The first is maximum a posteriori (MAP) inference, which aims to find the single most probable x .

An alternative is the Bayesian framework, where the goal becomes generating plausible reconstructions by sampling from the posterior distribution $p(\mathbf{x}|\mathbf{y})$, where $p(\mathbf{x}|\mathbf{y})$ can be decomposed into the prior $p(\mathbf{x})$ and the likelihood $p(\mathbf{y}|\mathbf{x})$. MAP delivers fast optimization, but struggles with high noise and multimodal posteriors, easily converging to local minima. In contrast, the Bayesian approach samples from $p(\mathbf{x}|\mathbf{y})$ to generate plausible reconstructions, quantify uncertainty, and handle multimodality. Both approaches critically depend on powerful prior models like DMs that encode the complex statistical structure of complex data and prior knowledge.

Most diffusion-based approaches to IPs are based on the denoising diffusion probabilistic models (DDPM) framework (Ho et al., 2020; Song & Ermon, 2020). The framework consists of forward and reverse diffusion processes. The forward process gradually corrupts the clean images \mathbf{x}_0 towards standard Gaussian noise \mathbf{x}_T . This process can be described by a stochastic differential equation (SDE), $d\mathbf{x} = -\frac{\beta_t}{2}\mathbf{x}dt + \sqrt{\beta_t}d\mathbf{w}$, where \mathbf{w} is the standard Wiener process. In practice, the process is discretized via a variance schedule $\{\beta_t\}_{t=1}^T$, forming a Markov chain:

$$q(\mathbf{x}_{1:T}|\mathbf{x}_0) := \prod_{t=1}^T q(\mathbf{x}_t|\mathbf{x}_{t-1}), \quad q(\mathbf{x}_t|\mathbf{x}_{t-1}) := \mathcal{N}(\mathbf{x}_t; \sqrt{1-\beta_t}\mathbf{x}_{t-1}, \beta_t \mathbf{I}) \quad (2)$$

In order to generate clean images, the reverse process begins with a noisy sample $\mathbf{x}_T \sim \mathcal{N}(\mathbf{x}_T; \mathbf{0}, \mathbf{I})$, and recursively refines it according to the reverse SDE, $d\mathbf{x} = -\frac{\beta_t}{2}\mathbf{x}dt - \beta_t \nabla_{\mathbf{x}} \log p_t(\mathbf{x})dt + \sqrt{\beta_t}d\bar{\mathbf{w}}$, where $\bar{\mathbf{w}}$ is the time-reversed standard wiener process, and $p_t(\mathbf{x})$ is the marginal probability of the noisy manifold at time t . $\nabla_{\mathbf{x}} \log p_t(\mathbf{x})$ is called the score function and is usually approximated by a neural network θ trained through score-matching methods.

Using the same discretization, clean images can be generated from the prior using an iterative de-noising process.

$$p_{\theta}(\mathbf{x}_{0:T}) := p(\mathbf{x}_T) \prod_{t=1}^T p_{\theta}(\mathbf{x}_{t-1}|\mathbf{x}_t), \quad p_{\theta}(\mathbf{x}_{t-1}|\mathbf{x}_t) := \mathcal{N}(\mathbf{x}_{t-1}; \boldsymbol{\mu}_{\theta}(\mathbf{x}_t, t), \boldsymbol{\Sigma}_{\theta}(\mathbf{x}_t, t)) \quad (3)$$

Building on the DDPM framework, to accelerate the denoising process, Song et al. (2022a) proposes Denoising Diffusion Implicit Models (DDIM), which define a non-Markovian and fully deterministic forward/reverse process ($\beta_t = 0$). Unlike DDPM, which injects stochasticity at each step to improve robustness, DDIM iteratively maps the initial noise \mathbf{x}_T to a clean sample \mathbf{x}_0 via a deterministic trajectory. For our method, this property is particularly beneficial, as it allows us to consider the entire reverse process as a deterministic mapping from \mathbf{x}_T to \mathbf{x}_0 .

Among successful DM-based methods for inverse problems, DPS and its variants (Chung et al., 2023; Kawar et al., 2022; Wang et al., 2023; Song et al., 2023; Chung et al., 2022) are best-known reconstruction algorithms. But they suffer from approximation errors from Tweedie's formula corrections. To mitigate noise sensitivity, TMPD incorporates second-order information to correct the guidance trajectory; however, like other iterative methods, it relies on modifying intermediate states, which risks drifting off the learned manifold. SITCOM (Alkhouri et al., 2025b) operates on the noisy image at each diffusion step and enforces a triple-consistency constraint: data fidelity, backward consistency with the diffusion posterior mean, and forward consistency along the diffusion trajectory. DIP (Chihaoui & Favaro, 2025b) updates the initial noise \mathbf{x}_T with data fidelity gradients after the standard diffusion sampling process. DMPlug (Wang et al., 2024) proposes a noise-space formulation but treats inverse problems as optimization tasks, making it *sensitive to noise*. While early stopping can mitigate this, its criterion is task- and noise-dependent. At the high noise levels considered here, the optimizer often becomes *trapped in a local mode*, rendering early stopping ineffective. Similar behavior is observed in other Maximum a Posteriori (MAP) methods such as ReSample (Song et al., 2024), which optimizes directly in clean-image space (leading to noisy or blurry images under early stopping). DAPS (Zhang et al., 2024), despite being formulated as a posterior sampling method, uses a heuristic $\hat{\sigma}_y$ that is much smaller than its true value to strengthen the consistency of the measurement. This deviation from true posterior sampling makes DAPS effectively MAP-like, inheriting the same sensitivity to noise.

2.2 HAMILTONIAN MONTE CARLO (HMC)

Hamiltonian Monte Carlo (HMC) (Duane et al., 1987) is an MCMC (Metropolis et al., 1953) sampling method that utilizes a fictitious momentum variable and simulates Hamiltonian dynamics to

efficiently explore distant regions. Due to its superior scaling properties in high dimensions compared to other simpler Metropolis methods Brooks et al. (2011), HMC is particularly well suited for sampling in high-dimensional space, such as the $3 \times 256 \times 256$ pixel space of images.

The Hamiltonian is defined as $H = U + V$, where $U = -\log p(\mathbf{x})$ and $V = \frac{1}{2}\mathbf{v}^\top \mathbf{M}^{-1} \mathbf{v}$. Then, we discretize the trajectory using the leapfrog integrator. For a single leapfrog step with step size δ , we have

$$\mathbf{v}(t + \delta/2) = \mathbf{v}(t) - \frac{\delta}{2} \frac{\partial U}{\partial \mathbf{x}} \Big|_{\mathbf{x}(t)}, \quad (4)$$

$$\mathbf{x}(t + \delta) = \mathbf{x}(t) + \delta \mathbf{M}^{-1} \mathbf{v}(t + \delta/2), \quad (5)$$

$$\mathbf{v}(t + \delta) = \mathbf{v}(t + \delta/2) - \frac{\delta}{2} \frac{\partial U}{\partial \mathbf{x}} \Big|_{\mathbf{x}(t+\delta)}, \quad (6)$$

where $\mathbf{v}(0) \sim \mathcal{N}(\mathbf{v}; \mathbf{0}, \mathbf{M})$. This process is repeated L times to form a full trajectory. Due to a discretization error, the Hamiltonian is no longer preserved, which introduces bias and violates the detailed balance. To correct for this, a Metropolis-Hastings (MH) correction step is applied at the end of each trajectory with acceptance probability of $\alpha = \min(1, \exp(-H_1 + H_0))$, where H_0, H_1 denotes the initial and proposed Hamiltonian, respectively.

3 METHODOLOGY

In this section, we propose a posterior sampling method, Noise-space Hamiltonian Monte Carlo (N-HMC), to solve IPs with pretrained DMs. We show its derivation in Section 3.1 and discuss its robustness to measurement noise in Section 3.2. In Section 3.3, our method is modified to allow for unknown types and levels of measurement noise.

3.1 NOISE-SPACE HAMILTONIAN MONTE CARLO (N-HMC)

The goal in solving inverse problems is to sample from the posterior distribution $p(\mathbf{x}_0|\mathbf{y}) \propto p(\mathbf{x}_0)p(\mathbf{y}|\mathbf{x}_0)$. Since direct sampling from $p(\mathbf{x}_0)$ is intractable, pretrained diffusion models are employed to provide a powerful prior. Standard diffusion-based approaches draw $\mathbf{x}_T \sim p(\mathbf{x}_T)$ from a Gaussian noise prior and iteratively denoise through intermediate timesteps, aiming to sample from $p(\mathbf{x}_T | \mathbf{y}), p(\mathbf{x}_{T-1} | \mathbf{y}), \dots, p(\mathbf{x}_0 | \mathbf{y})$ in sequence. The key challenge is evaluating the intractable likelihood $p(\mathbf{y}|\mathbf{x}_t)$ at each intermediate timestep t . To address this, iterative guidance methods (Kawar et al., 2022; Wang et al., 2023; Chung et al., 2023; Song et al., 2023; Rozet et al., 2024; Song et al., 2024; Zhang et al., 2024) introduce approximations and apply likelihood corrections of $\mathbf{x}_t \leftarrow \mathbf{x}_t + \eta \nabla_{\mathbf{x}_t} \log p(\mathbf{y}|\mathbf{x}_t)$. However, these gradient-based corrections systematically push intermediate states \mathbf{x}_t away from the distribution on which the denoiser is trained, leading to what we refer to as the *manifold feasibility problem*. Following SITCOM (Alkhouri et al., 2025b), we formalize this issue as:

Definition 3.1 (Manifold Feasibility). *For a pretrained diffusion model, let $p_t(\mathbf{x}_t)$ denote the marginal distribution at noise level t , and let \mathcal{M}_t be its high-probability generative manifold. An inverse-problem solver maintains manifold feasibility if the intermediate states $\{\mathbf{x}_t\}$ fed into the denoiser remain close to \mathcal{M}_t for all t , ensuring the final reconstruction \mathbf{x}_0 lies on the learned data manifold.*

Geometrically, standard guidance methods update \mathbf{x}_t using the likelihood gradient $\nabla_{\mathbf{x}_t} \log p(\mathbf{y}|\mathbf{x}_t)$. In high-dimensional spaces, this gradient vector often contains components orthogonal to the local tangent space of the data manifold \mathcal{M}_t . Consequently, adding this gradient systematically pushes the state \mathbf{x}_t into low-probability regions (off-manifold), feeding out-of-distribution inputs to the denoiser and causing accumulated artifacts as shown in Figure 1 (a). To avoid such approximations, we propose posterior sampling by drawing from the initial noise space. The sampled noise is then unconditionally denoised to a clean image. We adopt unconditional DDIM for the denoising process, which treats the entire denoising trajectory as a deterministic mapping $\hat{\mathbf{x}}_0 = \mathcal{D}(\mathbf{x}_T)$, so the problem becomes evaluating the posterior distribution of noise (Xia et al., 2023), i.e., $p(\mathbf{x}_T|\mathbf{y})$. We refer to our approach as *noise-space sampling* because HMC updates are performed exclusively on the initial noise $\mathbf{x}_T \sim \mathcal{N}(0, I)$. This differs from image-space and iterative guidance methods that

directly modify intermediate states \mathbf{x}_t using measurement-consistency gradients. Sampling from the noise space offers two advantages: (i) the prior $p(\mathbf{x}_T)$ is a simple Gaussian distribution, and (ii) the likelihood $p(\mathbf{y}|\mathbf{x}_T) = p(\mathbf{y}|\mathcal{D}(\mathbf{x}_T))$ is directly accessible without intermediate approximations.

We use HMC for efficient posterior sampling in the noise space. To strictly justify our sampling objective, we formulate the inference process as a latent variable model where the initial noise \mathbf{x}_T is the sole latent variable. We treat the unconditional DDIM process with N steps as a deterministic parameterized generator function, denoted as $\mathcal{D} : \mathbb{R}^n \rightarrow \mathbb{R}^n$, which maps \mathbf{x}_T to a clean image $\hat{\mathbf{x}}_0 = \mathcal{D}(\mathbf{x}_T)$. Under this formulation, the measurement generation process is defined by $\mathbf{x}_T \xrightarrow{\mathcal{D}} \hat{\mathbf{x}}_0 \xrightarrow{\mathcal{A}, \eta} \mathbf{y}$. Consequently, the conditional distribution of \mathbf{y} given \mathbf{x}_T depends entirely on the generated image $\hat{\mathbf{x}}_0$. The likelihood term is thus mathematically exact: $p(\mathbf{y}|\mathbf{x}_T) = p(\mathbf{y}|\hat{\mathbf{x}}_0 = \mathcal{D}(\mathbf{x}_T)) = \mathcal{N}(\mathbf{y}; \mathcal{A}(\mathcal{D}(\mathbf{x}_T)), \sigma_y^2 \mathbf{I})$. This allows us to perform posterior sampling directly in the noise space using the exact gradient of the likelihood with respect to \mathbf{x}_T . Then we can compute the conditional score using Bayes' rule:

$$\nabla_{\mathbf{x}_T} \log p(\mathbf{x}_T|\mathbf{y}) = \nabla_{\mathbf{x}_T} \log p(\mathbf{x}_T) + \nabla_{\mathbf{x}_T} \log p(\mathbf{y}|\mathbf{x}_T). \quad (7)$$

Since \mathbf{x}_T is Gaussian noise in the DDIM framework, the first term is simply

$$\nabla_{\mathbf{x}_T} \log p(\mathbf{x}_T) = -\nabla_{\mathbf{x}_T} \frac{\|\mathbf{x}_T\|^2}{2} = -\mathbf{x}_T. \quad (8)$$

For the case of Gaussian measurement noise, if the noise level σ_y^2 is known, the likelihood term becomes

$$\nabla_{\mathbf{x}_T} \log p(\mathbf{y}|\mathbf{x}_T) = \nabla_{\mathbf{x}_T} \log p(\mathbf{y}|\mathcal{D}(\mathbf{x}_T)) = -\nabla_{\mathbf{x}_T} \frac{\|\mathbf{y} - \mathcal{A}(\mathcal{D}(\mathbf{x}_T))\|^2}{2\sigma_y^2}. \quad (9)$$

We define $p(\mathbf{y}|\mathbf{x}_T) = p(\mathbf{y}|\mathcal{D}(\mathbf{x}_T))$ by viewing the denoising trajectory as a deterministic mapping $\hat{\mathbf{x}}_0 = \mathcal{D}(\mathbf{x}_T)$. This term can be computed directly using automatic differentiation. Because $\mathcal{D}(\mathbf{x}_T)$ results from a multi-step denoising process, backpropagating through multiple score networks can be computationally expensive. Following Wang et al. (2024), we illustrate in Appendix A.9 that accurate samples can still be obtained with as few as two denoising steps.

Once the conditional score $\nabla_{\mathbf{x}_T} \log p(\mathbf{x}_T|\mathbf{y})$ is computed, our method proceeds with standard Hamiltonian Monte Carlo (HMC) sampling. We use the identity matrix as the mass matrix for momentum sampling. During implementation, we observed that the initial noise may lie in regions of very low posterior probability, which forces HMC to adopt a tiny step size in order to maintain a proper acceptance rate. To address this issue, we use an annealing schedule for σ_y , allowing \mathbf{x}_T to explore the noise space more freely with a larger step size in the start-up stage. Once σ_y gradually declines to the target level, posterior samples are collected. The complete procedure is summarized in Algorithm 1, along with the unconditional DDIM denoising process in Algorithm 2.

3.2 ROBUSTNESS TO MEASUREMENT NOISE

An additional benefit of N-HMC over MAP methods is that the Gaussian prior acts as a regularization term in the noise space, keeping the noise vector \mathbf{x}_T close to the hypersphere of radius \sqrt{n} . Therefore, N-HMC produces samples that are *robust to measurement noise*, as justified by Proposition 1. For simplicity, we assume Gaussian measurement noise and that the forward operator \mathcal{A} is approximately linear along the clean image manifold.

Proposition 1. Assume that the distribution of the decoded sample \mathbf{x}_0 around the ground truth \mathbf{x}_0^* is well-approximated by a Gaussian distribution $p_\theta(\hat{\mathbf{x}}_0) \approx \mathcal{N}(\hat{\mathbf{x}}_0; \mathbf{x}_0^*, \sigma_0^2 \mathbf{I}_n)$. Then, the residual $\mathbf{y} - \mathbf{A}\hat{\mathbf{x}}_0$ satisfies

$$\mathbb{E}_{(\hat{\mathbf{x}}_0, \mathbf{y}) \sim p_\theta(\hat{\mathbf{x}}_0, \mathbf{y}|\mathbf{x}_0^*)} \|\mathbf{y} - \mathbf{A}\hat{\mathbf{x}}_0\|^2 = \sigma_y^2 \text{tr}(\mathbf{B}\mathbf{B}^\top) + \text{tr}(\mathbf{A}\Sigma_{\text{post}}\mathbf{A}^\top),$$

where

$$\Sigma_{\text{post}} = \left(\frac{\mathbf{A}^\top \mathbf{A}}{\sigma_y^2} + \frac{\mathbf{I}_n}{\sigma_0^2} \right)^{-1}, \quad \mathbf{B} = \left(\mathbf{I}_m - \frac{\mathbf{A}\Sigma_{\text{post}}\mathbf{A}^\top}{\sigma_y^2} \right),$$

Algorithm 1: N-HMC

Require: # HMC iterations K , # leapfrog steps L , initial integration step size δ , measurement noise schedule $\{\sigma_{y,k}\}$, $\mathbf{x}_T, \mathbf{y}, \mathcal{A}, \gamma$

- 1: **for** $k = 0$ to $K - 1$ **do**
- 2: **repeat**
- 3: $\mathbf{p} \sim \mathcal{N}(\mathbf{0}, \mathbf{I})$ // Initial momentum
- 4: $\hat{\mathbf{x}}_0 = \text{DDIM}(\mathbf{x}_T)$
- 5: $H_0 = \frac{1}{2}\|\mathbf{x}_T\|^2 + \frac{1}{2\sigma_{y,k}^2}\|\mathbf{y} - \mathcal{A}(\hat{\mathbf{x}}_0)\|^2 + \frac{1}{2}\mathbf{p}^\top \mathbf{p}$ // Current Hamiltonian
- 6: $\mathbf{x}_T^* \leftarrow \mathbf{x}_T$ // Initialize proposal \mathbf{x}_T
- 7: **for** $l = 0$ to $L - 1$ **do**
- 8: $\mathbf{p} \leftarrow \mathbf{p} - \frac{\delta}{2} \left(\mathbf{x}_T^* + \frac{1}{2\sigma_{y,k}^2} \nabla_{\mathbf{x}_T^*} \|\mathbf{y} - \mathcal{A}(\hat{\mathbf{x}}_0^*)\|^2 \right)$ // Update momentum
- 9: $\mathbf{x}_T^* \leftarrow \mathbf{x}_T^* + \delta \mathbf{p}$ // Update \mathbf{x}_T^*
- 10: $\hat{\mathbf{x}}_0^* = \text{DDIM}(\mathbf{x}_T^*)$
- 11: $\mathbf{p} \leftarrow \mathbf{p} - \frac{\delta}{2} \left(\mathbf{x}_T^* + \frac{1}{2\sigma_{y,k}^2} \nabla_{\mathbf{x}_T^*} \|\mathbf{y} - \mathcal{A}(\hat{\mathbf{x}}_0^*)\|^2 \right)$ // Update momentum
- 12: **end for**
- 13: $H_1 = \frac{1}{2}\|\mathbf{x}_T^*\|^2 + \frac{1}{2\sigma_{y,k}^2}\|\mathbf{y} - \mathcal{A}(\hat{\mathbf{x}}_0^*)\|^2 + \frac{1}{2}\mathbf{p}^\top \mathbf{p}$ // Proposal Hamiltonian
- 14: $u \sim \text{Unif}(0, 1)$
- 15: **if** $u < \exp(H_0 - H_1)$ **then**
- 16: Accept proposal
- 17: **else**
- 18: $\delta \leftarrow \gamma \delta$ // Anneal step size δ
- 19: **end if**
- 20: **until** Proposal accepted
- 21: $\mathbf{x}_T \leftarrow \mathbf{x}_T^*$ // Accept the proposal
- 22: **end for**
- 23: **return** \mathbf{x}_T

and \mathbf{I}_m is the $m \times m$ identity matrix. m denotes the dimension of \mathbf{y} .

The expected residual decomposes into two contributions: a noise-dependent term that appears only when measurement noise is present, and a second term that persists in all settings due to intrinsic uncertainty of prior diffusion models. In Corollary 1.1 below, we show that both terms behave in a way that yields a residual whose magnitude matches the true measurement noise.

Corollary 1.1 Under the assumptions of Proposition 1, if $\sigma_0/\sigma_y \ll 1$, the residual $\mathbf{y} - \mathcal{A}(\hat{\mathbf{x}}_0)$ satisfies

$$\mathbb{E}_{(\hat{\mathbf{x}}_0, \mathbf{y}) \sim p_\theta(\hat{\mathbf{x}}_0, \mathbf{y} | \mathbf{x}_0^*)} \|\mathbf{y} - \mathcal{A}(\hat{\mathbf{x}}_0)\|^2 \rightarrow m\sigma_y^2.$$

In other words, the magnitude of residual aligns with the true known level of measurement noise, indicating that N-HMC remains robust and does not overfit to noise.

3.3 NOISE-ADAPTIVE NHMC

In practice, the type and level of measurement noise are often unknown, making the likelihood term $p(\mathbf{y} | \mathbf{x}_T)$ intractable. To address this, other methods usually have tunable hyperparameters that control the strength of the likelihood term or use task-specific early stopping criteria. Instead of this heuristic approach, we introduce a noise-adaptive sampling method, *NA-NHMC*, which extends N-HMC to the *unknown noise setting without any additional hyperparameter tuning*.

We treat the noise variance as a latent variable and adopt the Jeffreys prior, a principled noninformative choice due to its parameterization invariance. It is scale-invariant and represents maximal uncertainty about the noise level, making it appropriate when no prior information about σ_y is available. It can also be viewed as the limiting case of an Inverse-Gamma prior $\sigma_y^2 \sim \text{Inv-}\Gamma(\alpha, \beta)$ as $\alpha, \beta \rightarrow 0$. The Inverse-Gamma distribution is the conjugate prior for the variance of a Gaussian likelihood. Proposition 2 characterizes the resulting behavior under additional assumptions.

$$p(\sigma_y^2) \sim \frac{1}{\sigma_y^2}.$$

Proposition 2 Under the assumptions of Proposition 1 and that the pretrained diffusion model unconditionally generates images that lie on the high-quality manifold ($\sigma_0/\sigma_y \ll 1$), then the update rule of NA-NHMC follows:

$$\nabla_{\mathbf{x}_T} \log p(\mathbf{y} | \mathbf{x}_T)_{\text{NA-NHMC}} = -\frac{1}{2\sigma_y^2} \nabla_{\mathbf{x}_T} \|\mathbf{y} - \mathcal{A}(\mathcal{D}(\mathbf{x}_T))\|^2.$$

By marginalizing σ_y^2 , the likelihood term becomes

$$p(\mathbf{y} | \mathbf{x}_T) = \int_0^\infty p(\mathbf{y} | \mathbf{x}_T, \sigma_y^2) p(\sigma_y^2) d\sigma_y^2 \quad (10)$$

$$\propto \left(\frac{1}{2} \|\mathbf{y} - \mathcal{A}(\mathcal{D}(\mathbf{x}_T))\|^2 \right)^{-m/2}. \quad (11)$$

where m denotes the dimensionality of the measurement space. The derivation of this expression is provided in Appendix A.1. Substituting this marginalized likelihood into the N-HMC framework yields our proposed noise-adaptive Algorithm 3. Proposition 2 below shows that, with an appropriate measurement noise prior, the likelihood term $\nabla_{\mathbf{x}_T} \log p(\mathbf{y} | \mathbf{x}_T)$ of NA-NHMC is identical to that of N-HMC (with known noise level).

Figure 2 demonstrates Proposition 2 in practice. All experiments use an identical setup across different noise levels, highlighting that our method does not require any hyperparameter tuning for a specific noise level. Despite the absence of such tunable parameters, the estimated standard deviation of the measurement noise, computed as $\|\mathbf{y} - \mathcal{A}(\hat{\mathbf{x}}_0)\|/\sqrt{m}$, closely matches the true, unknown noise level σ_y . This confirms that NA-NHMC effectively adapts to varying noise without specific tuning. The complete NA-NHMC is summarized in Algorithm 3.

The flexibility of NA-NHMC goes beyond noise-level robustness. Although NA-NHMC is formulated assuming Gaussian measurement noise, experiments with alternative noise types (Section 4.3) show that the method remains effective across other common noise distributions, demonstrating its broader robustness.

4 EXPERIMENTS

Following previous approaches (Wang et al., 2024) (Zhang et al., 2024), we evaluate our method on two datasets: FFHQ 256 × 256 (Karras et al., 2019) and ImageNet 256 × 256 (Deng et al., 2009), using 100 images from the validation set of each dataset. We utilize the same pretrained DM trained by Chung et al. (2023) for FFHQ and by Dhariwal & Nichol (2021) for ImageNet except for ReSample. For ReSample, we use a pretrained LDM by Rombach et al. (2022). All measurements are corrupted by additive Gaussian noise with standard deviation σ_y .

We compare our method against several representative baselines, including DiffPIR (Zhu et al., 2023), RED-diff (Mardani et al., 2023), DPS (Chung et al., 2023), DAPS (Zhang et al., 2024), ReSample (Song et al., 2024), SITCOM (Alkhouri et al., 2025b), and DMPlug (Wang et al., 2024). The implementation details for all the baseline methods are provided in Appendix A.5. We evaluate reconstruction quality using three standard metrics: peak signal-to-noise ratio (PSNR), structural similarity index measure (SSIM) (Wang et al., 2004), and Learned Perceptual Image Patch Similarity (LPIPS) (Zhang et al., 2018).

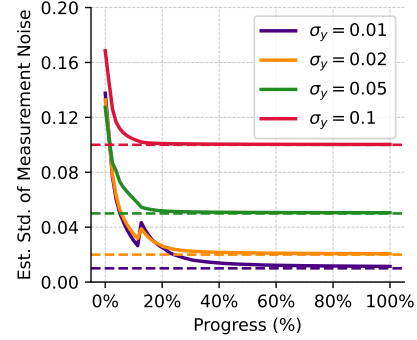


Figure 2: Gaussian deblur task on FFHQ (256 × 256) with varying measurement noise levels σ_y . The estimated standard deviation of measurement noise $\|\mathbf{y} - \mathcal{A}(\hat{\mathbf{x}}_0)\|/\sqrt{m}$ demonstrates that our noise-adaptive method accurately recovers the true σ_y (indicated by dashed line) without overfitting across different noise levels.

4.1 EXPERIMENT RESULTS

Linear IPs. We evaluate our approach on four linear inverse problems. For super-resolution tasks, we consider both $4\times$ and $16\times$ downsampling using 4×4 and 16×16 average pooling operations, respectively. We also examine random inpainting with 92% of pixels randomly masked, and anisotropic Gaussian deblurring using blur kernels with standard deviations of 20 and 1 in orthogonal directions. The results for linear IPs are presented in Tables 10-13.

Nonlinear IPs. We further assess performance on three challenging nonlinear inverse problems. The first is nonlinear deblurring using encoded blur kernels from Tran et al. (2021). The second is phase retrieval, where only the Fourier magnitude is observed as measurements. Finally, we consider HDR reconstruction, which aims to recover images with a higher dynamic range by a factor of 2 from tone-mapped observations. The results for nonlinear IPs are presented in Tables 1, 2, 14, 15.

Main Results. Our method achieves comparable or superior performance across most tasks, as measured by PSNR and SSIM on both the FFHQ and ImageNet datasets. Notably, the improvement over SOTA methods is more pronounced for nonlinear tasks, which are substantially more challenging than linear IPs. Many existing SOTA approaches are MAP-based by design (e.g., ReSample, SITCOM, and DMPlug) or become MAP-like heuristically (e.g., DAPS). While these methods perform well in low-noise regimes, they often overfit when the noise level is higher. Since the noise levels used in our experiments ($\sigma_y = 0.05, 0.20$) exceed those commonly reported in prior work, our results further demonstrate that the proposed noise-adaptive method is more robust and consistently outperforms alternatives across most tasks and metrics without any hyperparameter tuning. Figure 4 contains visual examples for the nonlinear deblurring problem. See Appendix A.12 for more examples. A fundamental distinction lies in the generalization capability across diverse degradation conditions. Standard guidance-based methods (e.g., DPS) inherently rely on manual hyperparameter calibration to balance measurement fidelity against the diffusion prior. As evidenced in Table 4, the optimal step size is highly task-dependent (ranging from $\zeta = 0.4$ to $\zeta = 10.0$), meaning a static configuration fails to generalize. In contrast, NA-NHMC derives its dynamics from the marginalized posterior, which effectively acts as an automatic gradient normalization mechanism. This structural advantage allows a single configuration to robustly generalize across varying tasks and noise levels without task-specific recalibration.

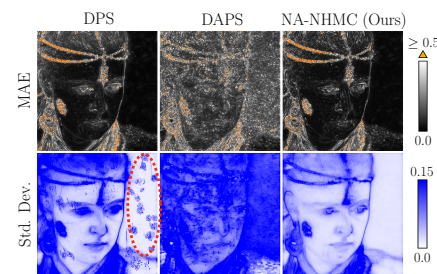


Figure 3: Comparative results are averaged over 100 independent runs. (Top) Mean absolute error (MAE) heatmaps. (Bottom) Standard deviation heatmaps across runs. Our method achieves the lowest standard deviation compared to DPS and DAPS, indicating reduced sensitivity to initialization.

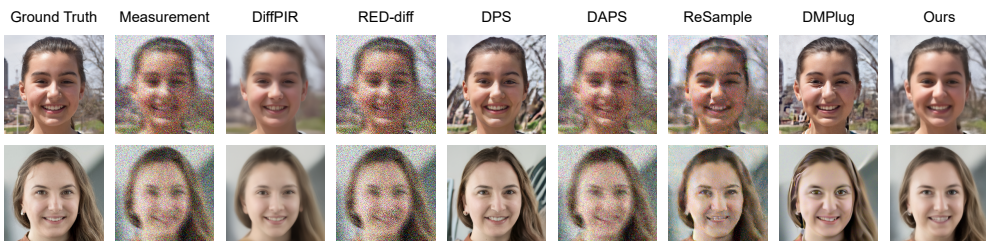


Figure 4: Nonlinear deblurring results on FFHQ (256×256) dataset with $\sigma_y = 0.2$. Visual comparison across state-of-the-art methods shows our approach produces high-quality reconstructions with sharp details and minimal artifacts.

4.2 HIGHLY ILL-POSED IPs: PHASE RETRIEVAL

Another challenge commonly faced by both MAP and sampling-based methods is becoming trapped in a local mode, particularly in highly multimodal IPs such as phase retrieval. Figure 5 illustrates this

issue. While DPS and DMPlug occasionally recover the correct solution, most initializations converge to spurious local modes and are thus counted as failures. In contrast, our method incorporates early exploration through σ_y scheduling, making it more robust to initialization and substantially more likely to recover the global solution.

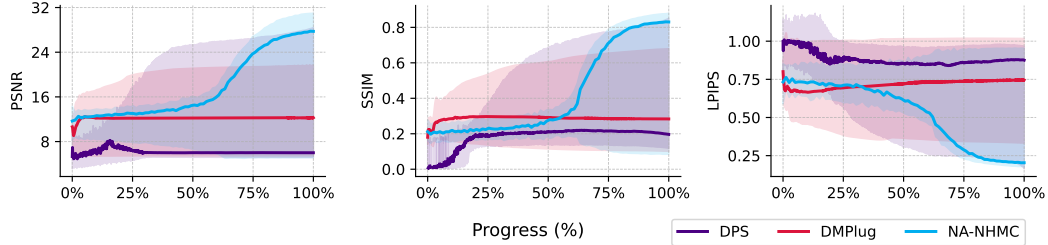


Figure 5: Phase retrieval task on FFHQ (256×256) with $\sigma_y = 0.01$. Each curve shows the median performance, with shaded areas denoting the 5th–95th percentile interval. Our method successfully solves the IP at a much higher rate than DPS and DMPlug. This is due to the annealing schedule of σ_y that allows for initial exploration of the noise space, resulting in a lower probability of being stuck on a local mode.

We quantify robustness to initialization using the standard deviation map in Figure 3. Our method achieves a mean absolute error (MAE) comparable to that of DPS, but with substantially lower pixel-wise standard deviation. While DPS can, on average, produce accurate reconstructions, its performance is sensitive to initialization and may introduce artifacts in both the face and background (red circle). In contrast, such artifacts never appear in any of the 100 runs with our method. Notably, despite exhibiting lower overall uncertainty, our method still assigns uncertainty in complex regions, which aligns with areas of high MAE (orange).

Table 1: Non-linear IPs Results on FFHQ (256×256) with Gaussian Noise $\sigma_y = 0.05$. (**Bold**: best, underline: second best)

	Nonlinear Deblurring			Phase Retrieval			HDR Reconstruction		
	PSNR \uparrow	SSIM \uparrow	LPIPS \downarrow	PSNR \uparrow	SSIM \uparrow	LPIPS \downarrow	PSNR \uparrow	SSIM \uparrow	LPIPS \downarrow
DiffPIR	26.12	0.743	0.289	16.77	<u>0.482</u>	0.543	25.20	0.814	0.223
RED-diff	18.12	0.217	0.680	11.83	0.213	0.769	21.44	0.525	0.458
DPS	23.26	0.672	0.300	10.87	0.296	0.714	<u>27.46</u>	0.849	0.168
DAPS	27.00	0.736	0.283	<u>18.52</u>	0.414	<u>0.528</u>	26.03	0.758	0.259
ReSample	24.57	0.637	0.432	13.95	0.377	0.677	23.65	0.722	0.386
SITCOM	24.97	0.569	0.328	11.89	0.216	0.723	26.97	0.753	0.256
DMPlug	<u>27.15</u>	0.784	0.266	-	-	-	25.17	0.783	0.260
NA-NHMC (ours)	27.66	0.792	0.249	19.30	0.554	0.482	28.45	0.849	0.217

Table 2: Non-linear IPs on ImageNet (256×256) with Gaussian Noise $\sigma_y = 0.05$. (**Bold**: best, underline: second best)

	Nonlinear Deblurring			HDR Reconstruction		
	PSNR \uparrow	SSIM \uparrow	LPIPS \downarrow	PSNR \uparrow	SSIM \uparrow	LPIPS \downarrow
DiffPIR	24.24	<u>0.638</u>	0.381	23.29	0.730	0.273
RED-diff	17.94	0.244	0.623	20.98	0.524	0.415
DPS	17.60	0.427	0.482	<u>25.31</u>	<u>0.763</u>	0.248
DAPS	<u>24.28</u>	0.632	0.404	23.57	0.709	0.283
SITCOM	24.00	0.556	<u>0.355</u>	24.76	0.708	0.276
DMPlug	22.30	0.576	0.421	20.61	0.562	0.431
NA-NHMC (ours)	24.98	0.694	0.308	25.86	0.779	<u>0.253</u>

4.3 ROBUSTNESS TO UNKNOWN MEASUREMENT NOISE

In practice, the measurement noise may be unknown and its type may not be Gaussian. This can pose a problem as many methods require multiple hyperparameters that are tuned for a specific level

and type of measurement noise. In this section, we evaluate our method’s robustness to unknown measurement noise on two tasks and two noise types: impulse and speckle. For impulse noise, each pixel in each channel is randomly replaced by 0 or 1 with a probability $p/2$ each, where $p \sim \text{Unif}(0, 0.2)$. For speckle noise, the noise takes the form $y(1 + \epsilon)$, where y is the measurement tensor and $\epsilon \sim \text{Unif}(0, 0.4)$. Table 3 shows that our method achieves superior performance on most metrics while using the exact same hyperparameters as the Gaussian noise experiment. As illustrated in Figure 6, methods such as DiffPIR, which do not suffer from noise overfitting in the Gaussian setting, now struggle with impulse noise. In contrast, even under high noise levels, NA-NHMC remains robust, producing high-quality reconstructions.

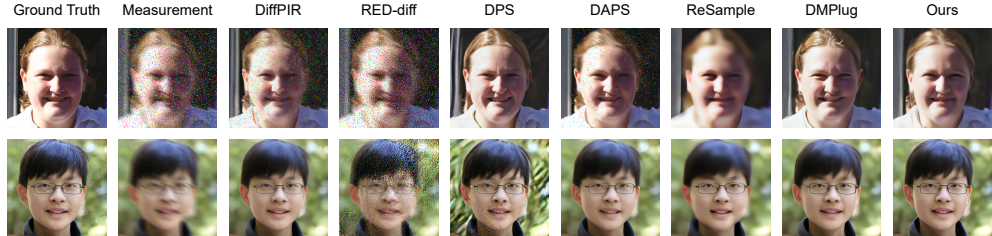


Figure 6: Nonlinear deblurring results on FFHQ (256×256) dataset under different noise conditions. (Top) Impulse noise. (Bottom) Speckle noise.

Table 3: The Performance Comparison with Different Types and Levels of Measurement Noise on FFHQ (256×256). (**Bold**: best, underline: second best)

	Super Resolution ($\times 4$)						Nonlinear Deblurring					
	Impulse			Speckle			Impulse			Speckle		
	PSNR \uparrow	SSIM \uparrow	LPIPS \downarrow	PSNR \uparrow	SSIM \uparrow	LPIPS \downarrow	PSNR \uparrow	SSIM \uparrow	LPIPS \downarrow	PSNR \uparrow	SSIM \uparrow	LPIPS \downarrow
DiffPIR	19.54	0.492	0.549	25.91	0.733	0.324	21.00	0.402	0.526	25.96	0.731	0.299
RED-diff	15.15	0.341	0.692	21.81	0.481	0.516	13.82	0.109	0.781	18.59	0.269	0.650
DPS	21.99	0.581	<u>0.395</u>	<u>27.00</u>	<u>0.761</u>	0.246	21.64	0.595	<u>0.322</u>	23.42	0.678	0.302
DAPS	15.00	0.361	0.702	24.48	0.597	0.442	17.94	0.259	0.657	26.46	0.698	0.308
ReSample	22.98	0.639	0.483	26.17	0.733	0.387	22.74	0.616	0.471	24.64	0.692	0.409
SITCOM	16.56	0.392	0.628	23.16	0.600	0.425	17.92	0.259	0.612	<u>26.49</u>	0.667	<u>0.295</u>
DMPlug	19.52	0.358	0.562	26.79	0.689	0.336	<u>23.79</u>	<u>0.662</u>	0.335	25.82	<u>0.740</u>	0.308
NA-NHMC (ours)	23.42	<u>0.631</u>	0.382	27.36	0.768	<u>0.290</u>	24.16	0.677	0.319	27.97	0.796	0.253

5 CONCLUSION

In this work, we introduce N-HMC, a posterior sampler that operates in the noise space using reverse diffusion as a deterministic mapping from initial noise to a clean image, enabling posterior exploration while keeping proposals on the learned data manifold. The developed noise-adaptive variant, NA-NHMC, eliminates task-specific hyperparameter tuning by automatically adapting to unknown noise types and levels, which is a significant practical advantage over existing approaches. Theory establishes the correctness and efficiency of noise-space sampling, and experiments across diverse linear and nonlinear inverse problems on FFHQ and ImageNet show state-of-the-art reconstructions, robustness to initialization and noise, competitive runtimes with a few denoising steps, and uncertainty-aware estimates. The provided analysis and experiments also show that our method can mitigate measurement-consistency drift, noise overfitting, and local-mode collapse without relying on any task-specific hyperparameter tuning.

While NA-NHMC shows promising results, it incurs higher computational cost compared to other methods such as DPS due to HMC sampling. Additionally, its reliance on a small number of diffusion steps may limit its immediate applicability to more complex applications. Moreover, the high dimensionality of the posterior leads to long warmup phases before reaching stationarity. Future work could address these challenges by developing more efficient gradient estimation techniques and incorporating faster warmup strategies that relax the requirement of exact detailed balance.

ACKNOWLEDGMENT

This research was supported by RIE2025 Human Health and Potential (HHP) Industry Alignment Fund Pre-Positioning Programme (IAF-PP) (Grant No. H24J4a0145). We gratefully acknowledge the insightful comments and suggestions provided by the anonymous reviewers.

REFERENCES

- Ismail Alkhouri, Shijun Liang, Cheng-Han Huang, Jimmy Dai, Qing Qu, Saiprasad Ravishankar, and Rongrong Wang. Sitcom: Step-wise triple-consistent diffusion sampling for inverse problems, 2025a. URL <https://arxiv.org/abs/2410.04479>.
- Ismail Alkhouri, Shijun Linag, Cheng-Han Huang, Jimmy Dai, Qing Qu, Saiprasad Ravishankar, and Rongrong Wang. Sitcom: Step-wise triple-consistent diffusion sampling for inverse problems. In *International Conference on Machine Learning (ICML)*, 2025b.
- Benjamin Boys, Mark Girolami, Jakiw Pidstrigach, Sebastian Reich, Alan Mosca, and O. Deniz Akyildiz. Tweedie moment projected diffusions for inverse problems, 2024. URL <https://arxiv.org/abs/2310.06721>.
- Steve Brooks, Andrew Gelman, Galin Jones, and Xiao-Li Meng. *Handbook of Markov Chain Monte Carlo*. Chapman and Hall/CRC, May 2011. ISBN 9780429138508. doi: 10.1201/b10905. URL <http://dx.doi.org/10.1201/b10905>.
- Hamadi Chihoui and Paolo Favaro. Diffusion image prior. *arXiv preprint arXiv:2503.21410v1*, 2025a. URL <https://arxiv.org/abs/2503.21410>. cs.CV.
- Hamadi Chihoui and Paolo Favaro. Diffusion image prior. In *Proceedings of the IEEE/CVF International Conference on Computer Vision (ICCV)*, pp. 24636–24644, October 2025b.
- Jiayue Chu, Chenhe Du, Xiyue Lin, Xiaoqun Zhang, Lihui Wang, Yuyao Zhang, and Hongjiang Wei. Highly accelerated mri via implicit neural representation guided posterior sampling of diffusion models. *Medical Image Analysis*, 100:103398, 2025. ISSN 1361-8415. doi: <https://doi.org/10.1016/j.media.2024.103398>. URL <https://www.sciencedirect.com/science/article/pii/S1361841524003232>.
- Hyungjin Chung, Byeongsu Sim, Dohoon Ryu, and Jong Chul Ye. Improving diffusion models for inverse problems using manifold constraints. *Advances in Neural Information Processing Systems*, 35:25683–25696, 2022.
- Hyungjin Chung, Jeongsol Kim, Michael Thompson Mccann, Marc Louis Klasky, and Jong Chul Ye. Diffusion posterior sampling for general noisy inverse problems. In *The Eleventh International Conference on Learning Representations*, 2023. URL <https://openreview.net/forum?id=OnD9zGAGT0k>.
- Duy-Phuong Dao, Hyung-Jeong Yang, and Jahae Kim. Conditional diffusion model for longitudinal medical image generation, 2024. URL <https://arxiv.org/abs/2411.05860>.
- Giannis Daras, Hyungjin Chung, Chieh-Hsin Lai, Yuki Mitsufuji, Jong Chul Ye, Peyman Milanfar, Alexandros G. Dimakis, and Mauricio Delbracio. A survey on diffusion models for inverse problems, 2024. URL <https://arxiv.org/abs/2410.00083>.
- Jia Deng, Wei Dong, Richard Socher, Li-Jia Li, Kai Li, and Li Fei-Fei. Imagenet: A large-scale hierarchical image database. In *2009 IEEE Conference on Computer Vision and Pattern Recognition*, pp. 248–255, 2009. doi: 10.1109/CVPR.2009.5206848.
- Prafulla Dhariwal and Alex Nichol. Diffusion models beat gans on image synthesis, 2021. URL <https://arxiv.org/abs/2105.05233>.
- Simon Duane, Anthony D Kennedy, Brian J Pendleton, and Duncan Roweth. Hybrid monte carlo. *Physics letters B*, 195(2):216–222, 1987.

- Jonathan Ho, Ajay Jain, and Pieter Abbeel. Denoising diffusion probabilistic models, 2020. URL <https://arxiv.org/abs/2006.11239>.
- Joel Janai, Fatma Güney, Aseem Behl, and Andreas Geiger. Computer vision for autonomous vehicles: Problems, datasets and state of the art, 2021. URL <https://arxiv.org/abs/1704.05519>.
- Tero Karras, Samuli Laine, and Timo Aila. A style-based generator architecture for generative adversarial networks, 2019. URL <https://arxiv.org/abs/1812.04948>.
- Tero Karras, Samuli Laine, Miika Aittala, Janne Hellsten, Jaakko Lehtinen, and Timo Aila. Analyzing and improving the image quality of stylegan, 2020. URL <https://arxiv.org/abs/1912.04958>.
- Bahjat Kawar, Michael Elad, Stefano Ermon, and Jiaming Song. Denoising diffusion restoration models. In Alice H. Oh, Alekh Agarwal, Danielle Belgrave, and Kyunghyun Cho (eds.), *Advances in Neural Information Processing Systems*, 2022. URL <https://openreview.net/forum?id=kxXvopt9pWK>.
- Morteza Mardani, Jiaming Song, Jan Kautz, and Arash Vahdat. A variational perspective on solving inverse problems with diffusion models, 2023. URL <https://arxiv.org/abs/2305.04391>.
- Nicholas Metropolis, Arianna W Rosenbluth, Marshall N Rosenbluth, Augusta H Teller, and Edward Teller. Equation of state calculations by fast computing machines. *Journal of Chemical Physics*, 21(6):1087–1092, 1953.
- Jeffrey Ouyang-Zhang, Daniel J. Diaz, Adam R. Klivans, and Philipp Krähenbühl. Predicting a protein’s stability under a million mutations, 2023. URL <https://arxiv.org/abs/2310.12979>.
- Weize Quan, Jiaxi Chen, Yanli Liu, Dong-Ming Yan, and Peter Wonka. Deep learning-based image and video inpainting: A survey, 2024. URL <https://arxiv.org/abs/2401.03395>.
- Robin Rombach, Andreas Blattmann, Dominik Lorenz, Patrick Esser, and Björn Ommer. High-resolution image synthesis with latent diffusion models, 2022. URL <https://arxiv.org/abs/2112.10752>.
- François Rozet, Gérôme Andry, Francois Lanusse, and Gilles Louppe. Learning diffusion priors from observations by expectation maximization. In *The Thirty-eighth Annual Conference on Neural Information Processing Systems*, 2024. URL <https://openreview.net/forum?id=7v88Fh6iSM>.
- Bowen Song, Soo Min Kwon, Zecheng Zhang, Xinyu Hu, Qing Qu, and Liyue Shen. Solving inverse problems with latent diffusion models via hard data consistency. In *The Twelfth International Conference on Learning Representations*, 2024. URL <https://openreview.net/forum?id=j8hdRqOUhN>.
- Jiaming Song, Chenlin Meng, and Stefano Ermon. Denoising diffusion implicit models, 2022a. URL <https://arxiv.org/abs/2010.02502>.
- Jiaming Song, Arash Vahdat, Morteza Mardani, and Jan Kautz. Pseudoinverse-guided diffusion models for inverse problems. In *International Conference on Learning Representations*, 2023. URL https://openreview.net/forum?id=9_gsMA8MRKQ.
- Yang Song and Stefano Ermon. Generative modeling by estimating gradients of the data distribution, 2020. URL <https://arxiv.org/abs/1907.05600>.
- Yang Song, Liyue Shen, Lei Xing, and Stefano Ermon. Solving inverse problems in medical imaging with score-based generative models, 2022b. URL <https://arxiv.org/abs/2111.08005>.

- Phong Tran, Anh Tuan Tran, Quynh Phung, and Minh Hoai. Explore image deblurring via encoded blur kernel space. In *2021 IEEE/CVF Conference on Computer Vision and Pattern Recognition (CVPR)*, pp. 11951–11960, 2021. doi: 10.1109/CVPR46437.2021.01178.
- Hengkang Wang, Xu Zhang, Taihui Li, Yuxiang Wan, Tiancong Chen, and Ju Sun. DMPlug: A plug-in method for solving inverse problems with diffusion models. In *The Thirty-eighth Annual Conference on Neural Information Processing Systems*, 2024. URL <https://openreview.net/forum?id=81IFFsfQUj>.
- Yinhuai Wang, Jiwen Yu, and Jian Zhang. Zero-shot image restoration using denoising diffusion null-space model. In *The Eleventh International Conference on Learning Representations*, 2023. URL <https://openreview.net/forum?id=mRieQgMtNTQ>.
- Zhou Wang, A.C. Bovik, H.R. Sheikh, and E.P. Simoncelli. Image quality assessment: from error visibility to structural similarity. *IEEE Transactions on Image Processing*, 13(4):600–612, 2004. doi: 10.1109/TIP.2003.819861.
- Yingzhi Xia and Nicholas Zabaras. Bayesian multiscale deep generative model for the solution of high-dimensional inverse problems. *Journal of Computational Physics*, 455:111008, 2022.
- Yingzhi Xia, Qifeng Liao, and Jinglai Li. Vi-dgp: A variational inference method with deep generative prior for solving high-dimensional inverse problems. *Journal of Scientific Computing*, 97(1):16, 2023.
- Zhihang Xu, Yingzhi Xia, and Qifeng Liao. A domain-decomposed vae method for bayesian inverse problems. *International Journal for Uncertainty Quantification*, 14(3), 2024.
- Kevin K. Yang, Zachary Wu, and Frances H. Arnold. Machine learning-guided directed evolution for protein engineering, 2019. URL <https://arxiv.org/abs/1811.10775>.
- Kai Yi, Bingxin Zhou, Yiqing Shen, Pietro Liò, and Yu Guang Wang. Graph denoising diffusion for inverse protein folding, 2023. URL <https://arxiv.org/abs/2306.16819>.
- Bingliang Zhang, Wenda Chu, Julius Berner, Chenlin Meng, Anima Anandkumar, and Yang Song. Improving diffusion inverse problem solving with decoupled noise annealing. *CoRR*, abs/2407.01521, 2024. URL <https://doi.org/10.48550/arXiv.2407.01521>.
- Jiawei Zhang, Ziyuan Liu, Leon Yan, Gen Li, and Yuantao Gu. Improving diffusion-based inverse algorithms under few-step constraint via learnable linear extrapolation, 2025. URL <https://arxiv.org/abs/2503.10103>.
- Richard Zhang, Phillip Isola, Alexei A. Efros, Eli Shechtman, and Oliver Wang. The unreasonable effectiveness of deep features as a perceptual metric. In *2018 IEEE/CVF Conference on Computer Vision and Pattern Recognition*, pp. 586–595, 2018. doi: 10.1109/CVPR.2018.00068.
- Hongkai Zheng, Wenda Chu, Bingliang Zhang, Zihui Wu, Austin Wang, Berthy T Feng, Caifeng Zou, Yu Sun, Nikola Kovachki, Zachary E Ross, et al. Inversebench: Benchmarking plug-and-play diffusion priors for inverse problems in physical sciences. *arXiv preprint arXiv:2503.11043*, 2025.
- Yuanzhi Zhu, Kai Zhang, Jingyun Liang, Jiezhang Cao, Bihan Wen, Radu Timofte, and Luc Van Gool. Denoising diffusion models for plug-and-play image restoration, 2023. URL <https://arxiv.org/abs/2305.08995>.

ETHICS STATEMENT

We affirm adherence to the ICLR Code of Ethics. This work uses publicly available datasets and standard benchmarks; no human subjects, personal data, or sensitive attributes are collected or processed. We assessed potential risks (misuse, bias, fairness, privacy, and security) and found none beyond those commonly associated with generic image/model evaluation. All institutional and legal requirements were respected, and we disclose that we have no conflicts of interest or external sponsorship that could unduly influence the results.

REPRODUCIBILITY STATEMENT

We provide implementation details, hyperparameters, and training/evaluation protocols in the main text and appendix; key equations and assumptions are stated with complete proofs in the appendix. All datasets and preprocessing steps are described and referenced; code and configuration files will be released in an anonymous repository as supplementary material to enable exact reproduction of results. Where applicable, we reference the specific sections, tables, and figures that document model architectures, inference procedures, and evaluation metrics.

A APPENDIX

A.1 ROBUST-N-HMC DERIVATION

Assumptions

1. Measurement noise $\eta \in \mathbb{R}^m$ follows gaussian distribution with unknown σ_y^2 :

$$p(\mathbf{y}|\mathbf{x}_T, \sigma_y^2) = \frac{1}{(2\pi\sigma_y^2)^{m/2}} \exp\left[-\frac{\|\mathbf{y} - \mathcal{A}(\mathcal{D}(\mathbf{x}_T))\|^2}{2\sigma_y^2}\right]. \quad (12)$$

2. σ_y follows a Jeffreys prior distribution:

$$p(\sigma_y^2) \propto \frac{1}{\sigma_y^2}. \quad (13)$$

Marginalizing σ_y^2 yields

$$p(\mathbf{y}|\mathbf{x}_T) = \int_0^\infty p(\mathbf{y}|\mathbf{x}_T, \sigma_y^2) p(\sigma_y^2) d\sigma_y^2 \quad (14)$$

$$\propto \int_0^\infty \frac{1}{(2\pi\sigma_y^2)^{m/2}} \exp\left[-\frac{\|\mathbf{y} - \mathcal{A}(\mathcal{D}(\mathbf{x}_T))\|^2}{2\sigma_y^2}\right] \frac{1}{\sigma_y^2} d\sigma_y^2 \quad (15)$$

$$\propto \int_0^\infty (\sigma_y^2)^{-\frac{m}{2}-1} \exp\left[-\frac{(1/2)\|\mathbf{y} - \mathcal{A}(\mathcal{D}(\mathbf{x}_T))\|^2}{\sigma_y^2}\right] d\sigma_y^2 \quad (16)$$

$$\propto \left(\frac{1}{2}\|\mathbf{y} - \mathcal{A}(\mathcal{D}(\mathbf{x}_T))\|^2\right)^{-m/2}. \quad (17)$$

And then, we have

$$\log p(\mathbf{y}|\mathbf{x}_T) = \left(-\frac{m}{2}\right) \log \left(\frac{1}{2}\|\mathbf{y} - \mathcal{A}(\mathcal{D}(\mathbf{x}_T))\|^2\right). \quad (18)$$

A.2 PROOFS

Measurement model. Let $\mathbf{x}_0^* \in \mathbb{R}^m$ denote the ground truth signal. The measurement is given by

$$\mathbf{y} = \mathcal{A}(\mathbf{x}_0^*) + \eta, \quad \eta \sim \mathcal{N}(0, \sigma_y^2 \mathbf{I}_m), \quad (19)$$

where $\mathcal{A} : \mathbb{R}^n \rightarrow \mathbb{R}^m$ is the measurement operator and η represents Gaussian measurement noise. In the following proofs, \mathcal{A} is assumed to be approximately linear around \mathbf{x}_0^* . Thus, $\mathcal{A}(\mathbf{x}_0) = \mathbf{A}\mathbf{x}_0$.

Generative model. Consider the DDIM sampler defined by

$$\hat{\mathbf{x}}_0 = \mathcal{D}(\mathbf{x}_T), \quad \mathbf{x}_T \sim \mathcal{N}(0, \mathbf{I}_n), \quad (20)$$

where \mathcal{D} denotes the deterministic decoder via the diffusion model.

Lemma 1. Product of two Gaussian probability density functions (PDFs).

$$q_1(\mathbf{x}) = \mathcal{N}(\mathbf{x}; \mu_1, \Sigma_1), \quad q_2(\mathbf{x}) = \mathcal{N}(\mathbf{x}; \mu_2, \Sigma_2).$$

Then, the product of $q_1(\mathbf{x})$ and $q_2(\mathbf{x})$ is proportional to a Gaussian PDF $\mathcal{N}(\mathbf{x}, \mu, \Sigma)$, where

$$\mu = \Sigma (\Sigma_1^{-1} \mu_1 + \Sigma_2^{-1} \mu_2), \quad \Sigma = (\Sigma_1^{-1} + \Sigma_2^{-1})^{-1}.$$

Lemma 2. Bias-variance decomposition of a random variable \mathbf{x} with mean μ and covariance matrix Σ , i.e.,

$$\mathbb{E}[\|\mathbf{x} - \mathbf{a}\|^2] = \|\mu - \mathbf{a}\|^2 + \text{tr}(\Sigma).$$

Proposition 1. Assume that the distribution of the decoded sample $\hat{\mathbf{x}}_0$ around the ground truth \mathbf{x}_0^* is well-approximated by a Gaussian distribution $p_\theta(\hat{\mathbf{x}}_0) \approx \mathcal{N}(\hat{\mathbf{x}}_0; \mathbf{x}_0^*, \sigma_0^2 \mathbf{I}_n)$. Then, the residual $\mathbf{y} - \mathbf{A}\hat{\mathbf{x}}_0$ satisfies

$$\mathbb{E}_{(\hat{\mathbf{x}}_0, \mathbf{y}) \sim p_\theta(\hat{\mathbf{x}}_0, \mathbf{y} | \mathbf{x}_0^*)} \|\mathbf{y} - \mathbf{A}\hat{\mathbf{x}}_0\|^2 = \sigma_y^2 \text{tr}(\mathbf{B}\mathbf{B}^\top) + \text{tr}(\mathbf{A}\Sigma_{\text{post}}\mathbf{A}^\top),$$

where

$$\Sigma_{\text{post}} = \left(\frac{\mathbf{A}^\top \mathbf{A}}{\sigma_y^2} + \frac{\mathbf{I}_n}{\sigma_0^2} \right)^{-1}, \quad \mathbf{B} = \left(\mathbf{I}_m - \frac{\mathbf{A}\Sigma_{\text{post}}\mathbf{A}^\top}{\sigma_y^2} \right).$$

Proof First, consider the distribution of $\hat{\mathbf{x}}_0$ given fixed \mathbf{x}_0^* and \mathbf{y}

$$p_\theta(\hat{\mathbf{x}}_0 | \mathbf{y}) \stackrel{(a)}{\propto} p_\theta(\mathbf{y} | \hat{\mathbf{x}}_0) p_\theta(\hat{\mathbf{x}}_0) \quad (21)$$

$$= \mathcal{N}(\mathbf{y}; \mathcal{A}(\hat{\mathbf{x}}_0), \sigma_y^2 \mathbf{I}_m) \mathcal{N}(\hat{\mathbf{x}}_0; \mathbf{x}_0^*, \sigma_0^2 \mathbf{I}_n) \quad (22)$$

$$\stackrel{(b)}{=} \mathcal{N}(\hat{\mathbf{x}}_0; (\mathbf{A}^\top \mathbf{A})^{-1} \mathbf{A}^\top \mathbf{y}, \sigma_y^2 (\mathbf{A}^\top \mathbf{A})^{-1}) \mathcal{N}(\hat{\mathbf{x}}_0; \mathbf{x}_0^*, \sigma_0^2 \mathbf{I}_n) \quad (23)$$

$$\stackrel{(c)}{=} \mathcal{N}(\hat{\mathbf{x}}_0; \boldsymbol{\mu}_{\text{post}}(\mathbf{y}), \boldsymbol{\Sigma}_{\text{post}}) \quad (24)$$

$$p_\theta(\mathbf{A}\hat{\mathbf{x}}_0 | \mathbf{y}) = \mathcal{N}(\hat{\mathbf{x}}_0; \mathbf{A}\boldsymbol{\mu}_{\text{post}}(\mathbf{y}), \mathbf{A}\boldsymbol{\Sigma}_{\text{post}}\mathbf{A}^\top), \quad (25)$$

where (a) follows from Bayes' theorem. (b) is from local linearity of \mathcal{A} . (c) is the result of Lemma 1 with

$$\boldsymbol{\mu}_{\text{post}}(\mathbf{y}) = \boldsymbol{\Sigma}_{\text{post}} \left(\frac{\mathbf{A}^\top \mathbf{y}}{\sigma_y^2} + \frac{\mathbf{x}_0^*}{\sigma_0^2} \right), \quad \boldsymbol{\Sigma}_{\text{post}} = \left(\frac{\mathbf{A}^\top \mathbf{A}}{\sigma_y^2} + \frac{\mathbf{I}_n}{\sigma_0^2} \right)^{-1}.$$

The expected squared residual conditioned on \mathbf{y} is

$$\mathbb{E}_{\hat{\mathbf{x}}_0 \sim p_\theta(\hat{\mathbf{x}}_0 | \mathbf{y})} \|\mathbf{y} - \mathbf{A}\hat{\mathbf{x}}_0\|^2 = \|\mathbf{y} - \mathbf{A}\boldsymbol{\mu}_{\text{post}}(\mathbf{y})\|^2 + \text{tr}(\mathbf{A}\boldsymbol{\Sigma}_{\text{post}}\mathbf{A}^\top), \quad (26)$$

which is the result of Lemma 2. Then, integrate over \mathbf{y} conditioned on \mathbf{x}_0^*

$$\mathbb{E}_{\hat{\mathbf{x}}_0, \mathbf{y} \sim p_\theta(\hat{\mathbf{x}}_0, \mathbf{y} | \mathbf{x}_0^*)} \|\mathbf{y} - \mathbf{A}\hat{\mathbf{x}}_0\|^2 \quad (27)$$

$$= \mathbb{E}_{\mathbf{y} \sim q(\mathbf{y} | \mathbf{x}_0^*)} [\mathbb{E}_{\hat{\mathbf{x}}_0 \sim p_\theta(\hat{\mathbf{x}}_0 | \mathbf{y})} \|\mathbf{y} - \mathbf{A}\hat{\mathbf{x}}_0\|^2] \quad (28)$$

$$= \mathbb{E}_{\mathbf{y} \sim q(\mathbf{y} | \mathbf{x}_0^*)} [\|\mathbf{y} - \mathbf{A}\boldsymbol{\mu}_{\text{post}}(\mathbf{y})\|^2 + \text{tr}(\mathbf{A}\boldsymbol{\Sigma}_{\text{post}}\mathbf{A}^\top)] \quad (29)$$

$$= \mathbb{E}_{\mathbf{y} \sim q(\mathbf{y} | \mathbf{x}_0^*)} \left[\left\| \left(\mathbf{I}_m - \frac{\mathbf{A}\boldsymbol{\Sigma}_{\text{post}}\mathbf{A}^\top}{\sigma_y^2} \right) \mathbf{y} - \frac{\mathbf{A}\boldsymbol{\Sigma}_{\text{post}}\mathbf{x}_0^*}{\sigma_0^2} \right\|^2 \right] + \text{tr}(\mathbf{A}\boldsymbol{\Sigma}_{\text{post}}\mathbf{A}^\top) \quad (30)$$

$$\stackrel{(a)}{=} \left\| \left(\mathbf{I}_m - \frac{\mathbf{A}\boldsymbol{\Sigma}_{\text{post}}\mathbf{A}^\top}{\sigma_y^2} \right) \mathbf{A}\mathbf{x}_0^* - \frac{\mathbf{A}\boldsymbol{\Sigma}_{\text{post}}\mathbf{x}_0^*}{\sigma_0^2} \right\|^2 + \text{tr}(\mathbf{B}(\sigma_y^2 \mathbf{I}_m)\mathbf{B}^\top) + \text{tr}(\mathbf{A}\boldsymbol{\Sigma}_{\text{post}}\mathbf{A}^\top) \quad (31)$$

$$= \sigma_y^2 \text{tr}(\mathbf{B}\mathbf{B}^\top) + \text{tr}(\mathbf{A}\boldsymbol{\Sigma}_{\text{post}}\mathbf{A}^\top), \quad (32)$$

where (a) is the result of Lemma 2, and $\mathbf{B} = \mathbf{I}_m - \frac{\mathbf{A}\boldsymbol{\Sigma}_{\text{post}}\mathbf{A}^\top}{\sigma_y^2}$.

Corollary 1.1 Under the assumptions of Proposition 1, if $\sigma_0/\sigma_y \ll 1$, the residual $\mathbf{y} - \mathcal{A}(\hat{\mathbf{x}}_0)$ satisfies

$$\mathbb{E}_{(\hat{\mathbf{x}}_0, \mathbf{y}) \sim p_\theta(\hat{\mathbf{x}}_0, \mathbf{y} | \mathbf{x}_0^*)} \|\mathbf{y} - \mathcal{A}(\hat{\mathbf{x}}_0)\|^2 \rightarrow m\sigma_y^2.$$

Proof If $\sigma_0/\sigma_y \ll 1$,

$$\boldsymbol{\Sigma}_{\text{post}} = \left(\frac{\mathbf{A}^\top \mathbf{A}}{\sigma_y^2} + \frac{\mathbf{I}_n}{\sigma_0^2} \right)^{-1} = \sigma_0^2 \left(\frac{\sigma_0^2 \mathbf{A}^\top \mathbf{A}}{\sigma_y^2} + \mathbf{I}_n \right)^{-1} \rightarrow \sigma_0^2 \mathbf{I}_n \quad (33)$$

$$\mathbf{B} = \mathbf{I}_m - \frac{\mathbf{A}\boldsymbol{\Sigma}_{\text{post}}\mathbf{A}^\top}{\sigma_y^2} \rightarrow \mathbf{I}_m - \frac{\sigma_0^2 \mathbf{A}\mathbf{A}^\top}{\sigma_y^2} \rightarrow \mathbf{I}_m \quad (34)$$

$$\mathbb{E} \|\mathbf{y} - \mathcal{A}(\hat{\mathbf{x}}_0)\|^2 = \sigma_y^2 \text{tr}(\mathbf{B}\mathbf{B}^\top) + \text{tr}(\mathbf{A}\boldsymbol{\Sigma}_{\text{post}}\mathbf{A}^\top) \rightarrow m\sigma_y^2 \quad (35)$$

Proposition 2 Under the assumptions of Proposition 1 and that the pre-trained diffusion model unconditionally generates images that lie on the high quality manifold ($\sigma_0/\sigma_y \ll 1$), then the update rule of NA-NHMC follows:

$$\nabla_{\mathbf{x}_T} \log p(\mathbf{y}|\mathbf{x}_T)_{\text{NA-NHMC}} = -\frac{1}{2\sigma_y^2} \nabla_{\mathbf{x}_T} \|\mathbf{y} - \mathcal{A}(\mathcal{D}(\mathbf{x}_T))\|^2$$

Proof We can consider the likelihood term of NA-NHMC

$$\log p(\mathbf{y}|\mathbf{x}_T) = \left(-\frac{m}{2}\right) \log \left(\frac{1}{2}\|\mathbf{y} - \mathcal{A}(\mathcal{D}(\mathbf{x}_T))\|^2\right) \quad (36)$$

$$\nabla_{\mathbf{x}_T} \log p(\mathbf{y}|\mathbf{x}_T) = \left(-\frac{m}{2\|\mathbf{y} - \mathcal{A}(\mathcal{D}(\mathbf{x}_T))\|^2}\right) \nabla_{\mathbf{x}_T} \|\mathbf{y} - \mathcal{A}(\mathcal{D}(\mathbf{x}_T))\|^2 \quad (37)$$

$$= \left(-\frac{1}{2\sigma_y^2}\right) \nabla_{\mathbf{x}_T} \|\mathbf{y} - \mathcal{A}(\mathcal{D}(\mathbf{x}_T))\|^2, \quad (38)$$

which follows from Corollary 1.1. This likelihood term is exactly the same as that of N-HMC, where the true noise level σ_y is known.

A.3 PSEUDOCODE OF UNCONDITIONAL DDIM

The DDIM method (Song et al., 2022a) we used in our experiment follows the Algorithm 2 below:

Algorithm 2: DDIM

```

Require: # diffusion steps  $T$ , diffusion model  $s_\theta$ , initial seed  $\mathbf{x}_T$ 
1: for  $t = T - 1$  to 0 do
2:    $\hat{\epsilon}_{t+1} = s_\theta(\mathbf{x}_{t+1}, t + 1)$  // Compute the score
3:    $\hat{\mathbf{x}}_0(\mathbf{x}_{t+1}) = \frac{1}{\sqrt{\bar{\alpha}_{t+1}}} (\mathbf{x}_{t+1} - \sqrt{1 - \bar{\alpha}_{t+1}} \hat{\epsilon}_{t+1})$  // Predict  $\hat{\mathbf{z}}_0$  with Tweedie's formula
4:    $\hat{\mathbf{x}}_t = \sqrt{\bar{\alpha}_t} \hat{\mathbf{x}}_0(\mathbf{x}_{t+1}) + \sqrt{1 - \bar{\alpha}_t} \hat{\epsilon}_{t+1}$  // Unconditional DDIM step
5: end for
6: return  $\mathbf{x}$ 

```

A.4 PSEUDOCODE OF THE NOISE-ADAPTIVE NHMC

Following the reasoning in Proposition 2, we assume an uninformative prior on σ_y . Under this assumption, the likelihood term can be written as

$$\log p(\mathbf{y}|\mathbf{x}_T) = \left(-\frac{m}{2}\right) \log \left(\frac{1}{2}\|\mathbf{y} - \mathcal{A}(\mathcal{D}(\mathbf{x}_T))\|^2\right).$$

where $m = \dim(\mathbf{y})$. The factor $1/2$ inside the logarithm can be omitted for the Hamiltonian and gradient computations. The corresponding gradient is

$$\nabla_{\mathbf{x}_T} \log p(\mathbf{y}|\mathbf{x}_T) = \left(-\frac{m}{2\|\mathbf{y} - \mathcal{A}(\mathcal{D}(\mathbf{x}_T))\|^2}\right) \nabla_{\mathbf{x}_T} \|\mathbf{y} - \mathcal{A}(\mathcal{D}(\mathbf{x}_T))\|^2$$

A.5 IMPLEMENTATION DETAILS FOR BASELINE METHODS

DiffPIR

Number of diffusion steps: 100

Number of optimization steps: 50

We follow the recommended hyperparameter $\eta = 1.0$ and $\lambda = 7.0$ from Zhang et al. (2025). The learning rate of the schedule-free AdamW optimizer is set to 0.1.

Algorithm 3: NA-NHMC

Require: # HMC iterations K , # leapfrog steps L , initial integration step size δ , $\mathbf{x}_T, \mathbf{y}, \mathcal{A}, \gamma$

- 1: **for** $k = 0$ to $K - 1$ **do**
- 2: **repeat**
- 3: $\mathbf{p} \sim \mathcal{N}(\mathbf{0}, \mathbf{I})$ // Initial momentum
- 4: $\hat{\mathbf{x}}_0 = \text{DDIM}(\mathbf{x}_T)$
- 5: $H_0 = \frac{1}{2}\|\mathbf{x}_T\|^2 + \frac{m}{2} \log(\|\mathbf{y} - \mathcal{A}(\hat{\mathbf{x}}_0)\|^2) + \frac{1}{2}\mathbf{p}^\top \mathbf{p}$ // Current Hamiltonian
- 6: $\mathbf{x}_T^* \leftarrow \mathbf{x}_T$ // Initialize proposal \mathbf{x}_T
- 7: **for** $l = 0$ to $L - 1$ **do**
- 8: $\mathbf{p} \leftarrow \mathbf{p} - \frac{\delta}{2} \left(\mathbf{x}_T^* + \frac{m}{2\|\mathbf{y} - \mathcal{A}(\hat{\mathbf{x}}_0^*)\|^2} \nabla_{\mathbf{x}_T^*} \|\mathbf{y} - \mathcal{A}(\hat{\mathbf{x}}_0^*)\|^2 \right)$ // Update momentum
- 9: $\mathbf{x}_T^* \leftarrow \mathbf{x}_T^* + \delta \mathbf{p}$ // Update \mathbf{x}_T^*
- 10: $\hat{\mathbf{x}}_0^* = \text{DDIM}(\mathbf{x}_T^*)$
- 11: $\mathbf{p} \leftarrow \mathbf{p} - \frac{\delta}{2} \left(\mathbf{x}_T^* + \frac{m}{2\|\mathbf{y} - \mathcal{A}(\hat{\mathbf{x}}_0^*)\|^2} \nabla_{\mathbf{x}_T^*} \|\mathbf{y} - \mathcal{A}(\hat{\mathbf{x}}_0^*)\|^2 \right)$ // Update momentum
- 12: **end for**
- 13: $H_1 = \frac{1}{2}\|\mathbf{x}_T^*\|^2 + \frac{m}{2} \log(\|\mathbf{y} - \mathcal{A}(\hat{\mathbf{x}}_0^*)\|^2) + \frac{1}{2}\mathbf{p}^\top \mathbf{p}$ // Proposal Hamiltonian
- 14: $u \sim \text{Unif}(0, 1)$
- 15: **if** $u < \exp(H_0 - H_1)$ **then**
- 16: Accept proposal
- 17: **else**
- 18: $\delta \leftarrow \gamma \delta$ // Anneal step size δ
- 19: **end if**
- 20: **until** Proposal accepted
- 21: $\mathbf{x}_T \leftarrow \mathbf{x}_T^*$ // Accept the proposal
- 22: **end for**
- 23: **return** \mathbf{x}_T

RED-diff

Number of optimization steps: 1000

We follow the recommended the hyperparameter $\lambda = 0.25$ and an Adam optimizer with $lr = 0.5$ as in Zhang et al. (2025)

DPS

Number of diffusion steps: 1000

We follow the learning rate form in Chung et al. (2023) with ζ_i adjusted for different tasks, as shown in Table 4.

Table 4: Tuned learning rate ζ_i for DPS

	SR ($\times 4$)	SR ($\times 16$)	Inpainting (92%)	Gaussian Deblurring	Nonlinear Deblurring	Phase Retrieval	HDR
FFHQ	1.0	0.6	1.0	1.0	1.0	0.4	1.0
ImageNet	1.0	0.6	1.0	0.4	0.5	-	1.0

DAPS

Number of diffusion steps: 250

Number of ODE solver steps: 4

We follow the hyperparameter settings of Zhang et al. (2024), as listed in Table 5, and adopt their heuristic $\sigma_y = 0.01$ in place of the actual value. $\delta = 0.01$ for all tasks. The number of MCMC sampling steps $N = 100$ for FFHQ (256×256) and $N = 40$ for ImageNet (256×256). Otherwise, the hyperparameter for each task is the same for both datasets.

ReSample

Number of diffusion steps: 500

Table 5: η_0 for DAPS

SR ($\times 4$)	SR ($\times 16$)	Inpainting (92%)	Gaussian Deblurring	Nonlinear Deblurring	Phase Retrieval	HDR
1e-4	1e-4	1e-4	1e-4	5e-5	5e-5	2e-5

For both noise levels ($\sigma_y = 0.05, 0.20$) tested in this paper, the recommended optimization steps lead to overfitting to noise and poor performance. Instead, we used 50 steps for pixel optimization and 25 steps for latent optimization.

SITCOM

Number of diffusion steps: 20

We follow the hyperparameter settings of Alkhouri et al. (2025a), as listed in Table 6. The stopping criterion δ for $\sigma_y \in \{0.05, 0.2\}$ is chosen as $0.051\sqrt{m}$ and $0.201\sqrt{m}$ respectively, with m denoting the dimension of y .

Table 6: Optimization Steps K for SITCOM

SR ($\times 4$)	SR ($\times 16$)	Inpainting (92%)	Gaussian Deblurring	Nonlinear Deblurring	Phase Retrieval	HDR
20	20	30	30	30	30	40

DMPPlug

Number of diffusion steps: 3

$$t = [250, 500, 750]$$

We set the Adam optimizer learning rate to 0.01. We follow the recommended stopping criteria in Wang et al. (2024). For linear tasks, we use a window size = 10, patience = 100, and a maximum iterations = 5000. For nonlinear tasks, we use the window size = 50 and patience = 300 with maximum iterations = 10000.

A.6 IMPLEMENTATION DETAILS FOR OUR METHOD

Number of diffusion steps: 2

$$t = [375, 750]$$

We implement NA-NHMC with the same hyperparameter configuration $L = 20$, $\delta_0 = 0.05$, $\gamma = 0.95$ for both datasets. For all tasks except phase retrieval, an initial step size $\delta_0 = 0.05$ and an annealing schedule $\sigma_{y,k} = 0.5 + 2(1 - k/10)$ is applied during the first 10 HMC iterations, after which, the noise-adaptive scheme (Algorithm 3) is used.

For phase retrieval, we use initial step size $\delta_0 = 0.2$ and keep other hyperparameters unchanged. An annealing schedule $\sigma_{y,k} = 1.0 + 20\sqrt{1 - k/50}$ is applied during the first 50 HMC iterations, after which, the noise-adaptive scheme (Algorithm 3) is used.

These annealing schedules are chosen to encourage sufficient exploration of the posterior in the early stage. Our results are not sensitive to the exact schedule: using a slower schedule does not degrade performance.

A.7 HYPERPARAMETER SENSITIVITY ANALYSIS

We evaluate several hyperparameter choices for the Hamiltonian Monte Carlo sampler on the super-resolution ($\times 4$) inverse problem using the FFHQ 256×256 dataset. When varying a particular hyperparameter, all remaining hyperparameters are kept at their default values used in all other experiments. For different choices of the number of leapfrog steps L , we also adjust the number of HMC iterations to ensure that each setting uses the same amount of computational resources. The

resulting performance is summarized in the tables below. The results indicate that the performance of NA-NHMC exhibits little sensitivity to the choice of hyperparameters.

Table 7: Different step sizes ϵ for Super Resolution ($\times 4$) on FFHQ (256×256) with Gaussian Noise $\sigma_y = 0.05$. (**Bold**: best)

	0.02	0.05	0.10	0.15	0.20
PSNR \uparrow	27.12	27.29	27.31	27.31	27.31
SSIM \uparrow	0.745	0.770	0.771	0.771	0.772
LPIPS \downarrow	0.299	0.291	0.288	0.288	0.286

Table 8: Different number of leapfrog steps L for Super Resolution ($\times 4$) on FFHQ (256×256) with Gaussian Noise $\sigma_y = 0.05$. (**Bold**: best)

	10	15	20	25	30
PSNR \uparrow	26.86	27.18	27.29	27.36	27.34
SSIM \uparrow	0.749	0.765	0.770	0.771	0.777
LPIPS \downarrow	0.318	0.299	0.291	0.286	0.281

Table 9: Step size decay factor γ for Super Resolution ($\times 4$) on FFHQ (256×256) with Gaussian Noise $\sigma_y = 0.05$. (**Bold**: best)

	0.91	0.93	0.95	0.97	0.99
PSNR \uparrow	27.29	27.31	27.29	27.31	27.30
SSIM \uparrow	0.770	0.769	0.770	0.771	0.770
LPIPS \downarrow	0.291	0.289	0.291	0.288	0.289

A.8 ADDITIONAL EXPERIMENT RESULTS

Linear IPs results

All experiments in Section 3.3 are repeated with a **higher level of Gaussian measurement noise** ($\sigma_y = 0.20$). The results are shown below.

A.9 ABLATION STUDIES

Number of HMC iterations

Sampling with HMC requires a warmup phase, since the initial noise x_T may be far from the solution. As shown in Figure 7, the quality of sampled images improves monotonically with the number of iterations, as expected. Performance begins to plateau after roughly 120 iterations. Unlike MAP-based methods such as ReSample (Song et al., 2024) and DMPlug (Wang et al., 2024), it does not deteriorate beyond this point. This stability provides evidence that the prior term acts as an effective regularizer, preventing overfitting.

Number of diffusion steps and memory usage

In this section, we evaluate NA-NHMC with varying numbers of diffusion steps, using fixed parameters $K = 80$ and $L = 20$. Both runtime (in seconds) and memory usage (in GB) increase linearly with the number of steps. We ran all experiments on NVIDIA H200 GPU. The baseline cost is 90 seconds and 3.63 GB for two steps, with each additional step adding roughly 45 seconds and 1.84 GB. The quantitative evaluations are shown in Figure 8. While three diffusion steps achieve the highest PSNR and lowest LPIPS, the improvement over two steps is marginal. To avoid incurring roughly 50% additional runtime and memory overhead, we use two diffusion steps in all experiments.

Note that performance appears to decline when using more than three diffusion steps. This effect arises because the sampler converges more slowly to its stationary distribution as the number of

Table 10: Linear IPs on FFHQ (256×256) with Gaussian Noise $\sigma_y = 0.05$. (**Bold**: best, underline: second best)

	Super Resolution ($\times 4$)			Super Resolution ($\times 16$)			Random Inpainting (92%)			Gaussian Deblurring		
	PSNR \uparrow	SSIM \uparrow	LPIPS \downarrow	PSNR \uparrow	SSIM \uparrow	LPIPS \downarrow	PSNR \uparrow	SSIM \uparrow	LPIPS \downarrow	PSNR \uparrow	SSIM \uparrow	LPIPS \downarrow
DiffPIR	25.96	0.735	0.322	19.84	<u>0.541</u>	0.444	20.93	0.595	0.405	27.48	0.778	0.287
RED-diff	21.58	0.390	0.602	17.60	<u>0.391</u>	0.567	23.70	0.651	0.344	17.07	0.213	0.692
DPS	26.84	0.762	0.239	20.06	0.522	0.380	25.74	0.745	0.245	26.88	0.761	0.234
DAPS	24.58	0.559	0.514	17.28	0.420	0.541	25.68	0.685	0.331	23.34	0.478	0.474
ReSample	26.18	0.737	0.382	20.01	0.532	0.576	24.12	0.599	0.442	25.98	0.728	0.385
SITCOM	27.35	0.787	<u>0.268</u>	<u>20.82</u>	0.574	<u>0.400</u>	<u>26.56</u>	0.785	<u>0.266</u>	<u>27.94</u>	<u>0.796</u>	0.266
DMPlug	26.73	0.697	0.321	17.42	0.280	0.607	26.15	0.769	0.270	27.81	0.769	0.289
NA-NHMC (ours)	<u>27.29</u>	<u>0.770</u>	0.291	20.85	0.531	0.452	26.72	0.785	0.268	28.36	0.798	<u>0.259</u>

Table 11: Linear IPs ImageNet (256×256) with Gaussian Noise $\sigma_y = 0.05$. (**Bold**: best, underline: second best)

	Super Resolution ($\times 4$)			Super Resolution ($\times 16$)			Random Inpainting (92%)			Gaussian Deblurring		
	PSNR \uparrow	SSIM \uparrow	LPIPS \downarrow	PSNR \uparrow	SSIM \uparrow	LPIPS \downarrow	PSNR \uparrow	SSIM \uparrow	LPIPS \downarrow	PSNR \uparrow	SSIM \uparrow	LPIPS \downarrow
DiffPIR	23.99	0.626	0.426	<u>18.48</u>	<u>0.387</u>	0.626	19.30	0.443	0.583	25.24	0.678	0.378
RED-diff	17.67	0.266	0.613	12.45	0.151	0.726	17.25	0.360	0.541	13.99	0.170	0.688
DPS	23.36	0.623	<u>0.345</u>	17.15	0.339	0.524	22.31	0.593	0.347	22.55	0.555	0.401
DAPS	23.86	0.568	0.461	14.29	0.139	0.753	23.23	0.585	0.432	24.52	0.558	0.423
SITCOM	<u>24.93</u>	0.684	<u>0.318</u>	18.58	0.404	0.525	<u>23.89</u>	0.684	<u>0.320</u>	<u>25.63</u>	0.712	0.311
DMPlug	24.52	<u>0.667</u>	0.378	16.74	0.311	0.590	23.49	0.668	0.358	23.55	0.605	0.433
NA-NHMC (ours)	24.99	0.665	0.355	19.09	0.396	<u>0.580</u>	24.10	0.676	<u>0.324</u>	25.76	0.699	<u>0.327</u>

Table 12: Linear IPs on FFHQ (256×256) with Gaussian Noise $\sigma_y = 0.20$. (**Bold**: best, underline: second best)

	Super Resolution ($\times 4$)			Super Resolution ($\times 16$)			Random Inpainting (92%)			Gaussian Deblurring		
	PSNR \uparrow	SSIM \uparrow	LPIPS \downarrow	PSNR \uparrow	SSIM \uparrow	LPIPS \downarrow	PSNR \uparrow	SSIM \uparrow	LPIPS \downarrow	PSNR \uparrow	SSIM \uparrow	LPIPS \downarrow
DiffPIR	21.22	0.591	0.417	16.09	0.420	0.551	17.83	0.470	0.509	24.29	0.683	0.355
RED-diff	12.64	0.101	0.824	11.49	0.152	0.799	15.33	0.168	0.731	8.47	0.037	0.868
DPS	21.80	0.556	<u>0.385</u>	16.13	0.377	<u>0.507</u>	21.60	0.531	<u>0.404</u>	24.45	0.678	0.290
DAPS	13.48	0.121	0.792	17.08	0.420	0.549	20.64	0.353	0.587	8.12	0.031	0.862
ReSample	22.95	0.632	0.501	17.93	<u>0.468</u>	0.661	22.62	0.615	0.535	24.60	0.682	0.438
SITCOM	<u>23.04</u>	0.647	0.362	<u>17.49</u>	0.469	0.495	<u>23.23</u>	<u>0.653</u>	0.359	<u>24.97</u>	<u>0.709</u>	<u>0.323</u>
DMPlug	15.95	0.140	0.706	11.69	0.093	0.773	19.65	0.347	0.564	17.33	0.181	0.660
NA-NHMC (ours)	23.29	<u>0.636</u>	0.391	17.36	0.393	0.552	23.69	0.670	<u>0.365</u>	25.57	0.710	0.327

Table 13: Linear IPs on ImageNet (256×256) with Gaussian Noise $\sigma_y = 0.20$. (**Bold**: best, underline: second best)

	Super Resolution ($\times 4$)			Super Resolution ($\times 16$)			Random Inpainting (92%)			Gaussian Deblurring		
	PSNR \uparrow	SSIM \uparrow	LPIPS \downarrow	PSNR \uparrow	SSIM \uparrow	LPIPS \downarrow	PSNR \uparrow	SSIM \uparrow	LPIPS \downarrow	PSNR \uparrow	SSIM \uparrow	LPIPS \downarrow
DiffPIR	19.90	0.448	0.577	18.48	0.387	0.626	16.91	0.295	0.684	22.38	0.550	0.493
RED-diff	11.35	0.097	0.776	9.29	0.098	0.811	11.37	0.079	0.782	8.08	0.043	0.817
DPS	19.29	0.406	<u>0.481</u>	11.25	0.145	0.728	18.64	0.361	0.505	20.33	0.455	0.468
DAPS	13.71	0.151	0.760	14.27	0.139	0.755	18.89	0.248	0.598	9.06	0.060	0.789
SITCOM	<u>20.87</u>	<u>0.490</u>	0.458	16.16	<u>0.325</u>	<u>0.628</u>	<u>20.90</u>	<u>0.494</u>	<u>0.457</u>	22.73	0.584	0.402
DMPlug	18.58	0.412	0.500	9.53	0.125	0.782	19.15	0.447	0.474	23.05	<u>0.591</u>	0.423
NA-NHMC (ours)	21.53	0.510	0.492	<u>16.43</u>	0.276	0.675	21.80	0.536	0.456	<u>23.45</u>	0.597	<u>0.405</u>

diffusion steps increases. While increasing the number of HMC iterations could offset this effect, it would further amplify runtime costs to an impractical level.

Diffusion schedule

The pre-trained DMs used in this paper have 1000 diffusion steps. While other methods usually use evenly-spaced schedule with the first step being pure Gaussian noise ($\bar{a}_t = 0$), we found this choice to be numerically unstable for our few-step setting. Since we are using two steps for unconditional DDIM, the natural choice is to use timesteps in the middle. Thus, we choose $t = [375, 750]$, which is spread evenly and avoids numerical stability. Table 16 confirms that this schedule yields superior performance in PSNR and SSIM while being close to optimal for LPIPS. We adopt this diffusion schedule for all main experiments.

Table 14: Non-linear IPs on FFHQ (256×256) with Gaussian Noise $\sigma_y = 0.20$. (**Bold**: best, underline: second best)

	Nonlinear Deblurring			Phase Retrieval			HDR Reconstruction		
	PSNR \uparrow	SSIM \uparrow	LPIPS \downarrow	PSNR \uparrow	SSIM \uparrow	LPIPS \downarrow	PSNR \uparrow	SSIM \uparrow	LPIPS \downarrow
DiffPIR	<u>23.34</u>	0.641	0.374	16.76	0.482	0.543	21.85	0.694	0.344
RED-diff	12.85	0.063	0.816	10.07	0.061	0.855	16.73	0.222	0.649
DPS	22.83	<u>0.643</u>	0.307	10.60	0.267	0.701	<u>24.92</u>	<u>0.703</u>	<u>0.321</u>
DAPS	17.38	0.154	0.728	12.93	0.103	0.797	18.04	0.299	0.607
ReSample	23.30	0.635	0.477	12.51	0.335	0.712	22.51	0.677	0.428
SITCOM	16.26	0.173	0.656	10.19	0.082	0.810	20.11	0.346	0.534
DMPlug	22.08	0.544	0.437	-	-	-	16.17	0.473	0.481
NA-NHMC (ours)	24.89	0.705	<u>0.317</u>	<u>16.17</u>	<u>0.434</u>	<u>0.570</u>	26.61	0.793	0.271

Table 15: Non-linear IPs on ImageNet (256×256) with Gaussian Noise $\sigma_y = 0.20$. (**Bold**: best, underline: second best)

	Nonlinear Deblurring			HDR Reconstruction		
	PSNR \uparrow	SSIM \uparrow	LPIPS \downarrow	PSNR \uparrow	SSIM \uparrow	LPIPS \downarrow
DiffPIR	21.52	0.492	0.526	19.94	0.556	<u>0.418</u>
RED-diff	12.47	0.071	0.759	16.46	0.267	<u>0.593</u>
DPS	16.11	0.340	0.551	21.92	0.519	0.448
DAPS	17.84	0.201	0.617	18.08	0.351	0.536
SITCOM	14.49	0.156	0.668	19.82	0.441	0.500
DMPlug	21.80	<u>0.561</u>	0.420	20.54	0.562	0.430
NA-NHMC (ours)	22.61	0.585	0.382	24.12	0.701	0.320

A.10 ALTERNATIVE SAMPLING SCHEMES

Sampling in a space as high-dimensional as $(3 \times 256 \times 256)$ is a challenging task. Many standard sampling algorithms are not suitable in this setting. A key requirement for efficiency is the use of gradient information to accelerate convergence. The simplest such method is the Unadjusted Langevin Algorithm (ULA).

However, because ULA lacks a Metropolis–Hastings (MH) correction, its step size must be tuned carefully. Figure 9 illustrates this trade-off: large step sizes enable rapid exploration but cause significant discretization error as σ_y approaches the target value, resulting in poor samples; conversely, small step sizes reduce error but lead to very slow exploration and long runtime.

Since different stages of the sampling chain require different effective step sizes, algorithms with a Metropolis–Hastings (MH) correction are more attractive, as the acceptance test provides a natural criterion for adapting step size. We therefore consider the Metropolis-Adjusted Langevin Algorithm (MALA), the No-U-Turn Sampler (NUTS), and Hamiltonian Monte Carlo (HMC). In practice, however, both MALA and NUTS tend to settle on excessively small step sizes in this high-dimensional setting, resulting in impractically long runtimes. By contrast, HMC accommodates larger step sizes and achieves a more favorable trade-off between accuracy and efficiency, making it the most suitable choice for our framework.

A.11 ALTERNATIVE PRIOR MODEL: GAN-BASED INFERENCE

In place of the diffusion models, we experimented with StyleGAN2 (Karras et al., 2020) as the prior model for FFHQ 256×256 dataset. The quantitative results are presented in Table 17. The quality of image samples are significantly inferior to diffusion models across all tasks.

A.12 ADDITIONAL QUALITATIVE RESULTS

In this section, we present additional qualitative results. Since we don’t have access to an LDM for ImageNet (256×256), ReSample cannot be applied to this dataset.

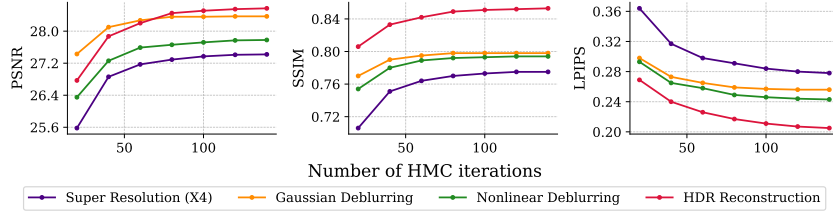


Figure 7: Performance of NA-NHMC across four tasks for FFHQ (256×256) as a function of the number of HMC iterations K . For all tasks, performance increases monotonically with more steps, but with diminishing improvements.

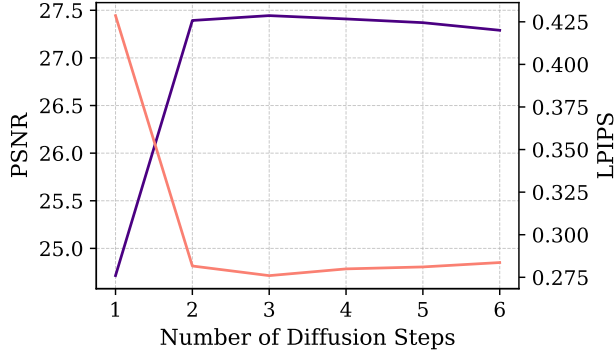


Figure 8: Performance of NA-NHMC on SR ($\times 4$) task for FFHQ (256×256) as a function of the number of diffusion steps. The initial step is fixed at $T = 750$ for all cases to avoid numerical instability, and the remaining steps are evenly spaced in $[0, 750]$.

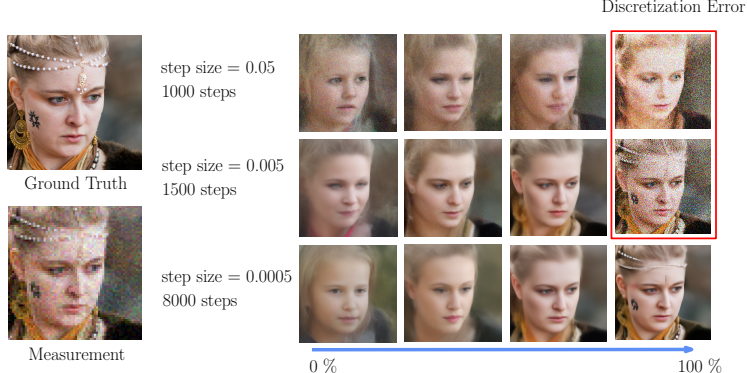


Figure 9: Unadjusted Langevin Algorithm (ULA) with different step sizes. Larger step sizes accelerate convergence but introduce greater discretization error, substantially degrading sample quality.

Table 16: Performance of NA-NHMC on SR ($\times 4$) for FFHQ (256×256). Each schedule is defined by two parameters: (i) the first timestep (rows: 600, 750, 900) and (ii) the final timestep (columns: 250, 375, 500).

Metrics	PSNR			SSIM			LPIPS		
	600	750	900	600	750	900	600	750	900
250	27.12	27.24	26.82	0.744	0.767	0.718	0.290	0.287	0.335
375	27.03	27.29	27.07	0.736	0.770	0.738	0.304	0.291	0.319
500	26.87	27.17	27.01	0.723	0.763	0.741	0.330	0.305	0.317

Table 17: GAN-Based Inference for Linear IPs on FFHQ (256×256) with Gaussian Noise $\sigma_y = 0.05$.

	Super Resolution ($\times 4$)			Random Inpainting (92%)		
	PSNR \uparrow	SSIM \uparrow	LPIPS \downarrow	PSNR \uparrow	SSIM \uparrow	LPIPS \downarrow
NA-NHMC (GAN)	18.27	0.454	0.513	17.80	0.440	0.528
NA-NHMC (DDIM)	27.29	0.770	0.291	26.72	0.785	0.268

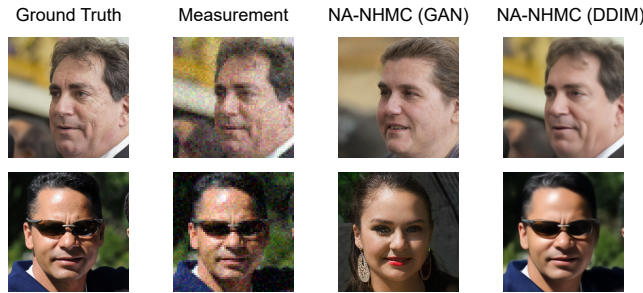


Figure 10: Comparison between GAN and Diffusion Model (DDIM) for SR($\times 4$). FFHQ (256×256). $\sigma_y = 0.05$.

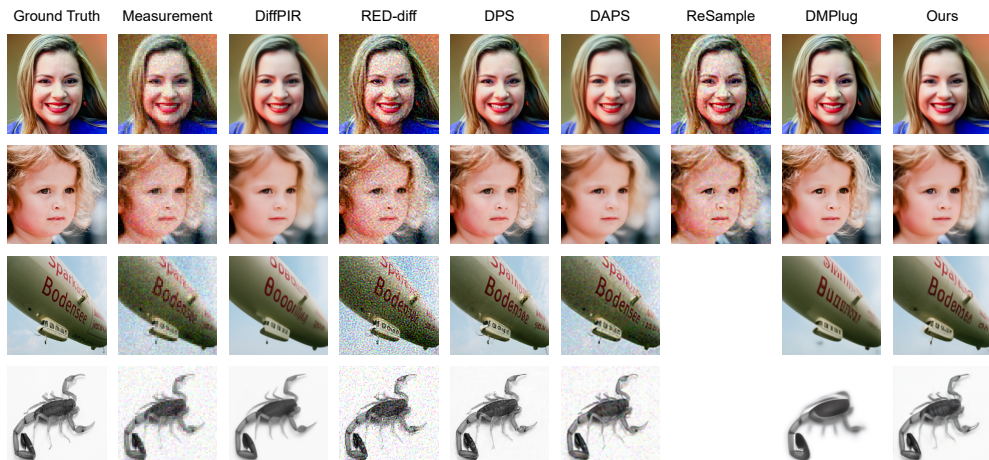


Figure 11: SR($\times 4$). (Top) FFHQ (256×256). (Bottom) ImageNet (256×256). $\sigma_y = 0.05$

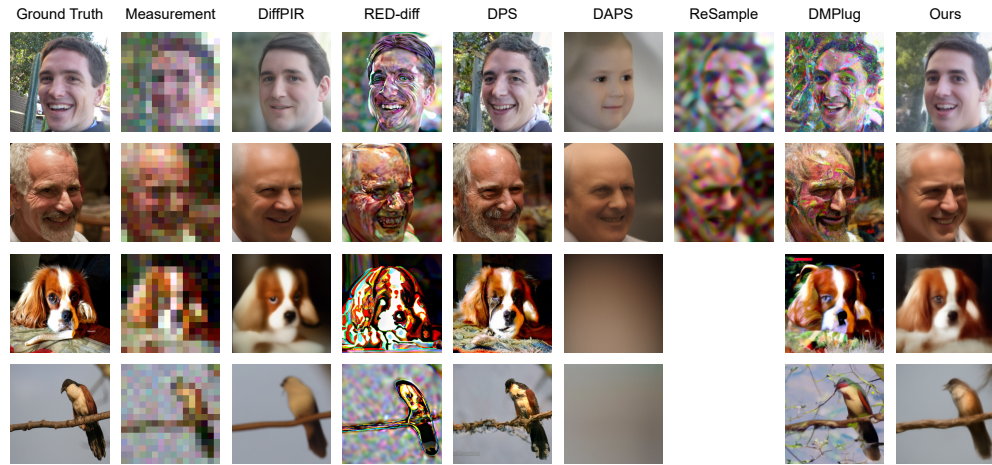


Figure 12: SR($\times 16$). (Top) FFHQ (256×256). (Bottom) ImageNet (256×256). $\sigma_y = 0.05$

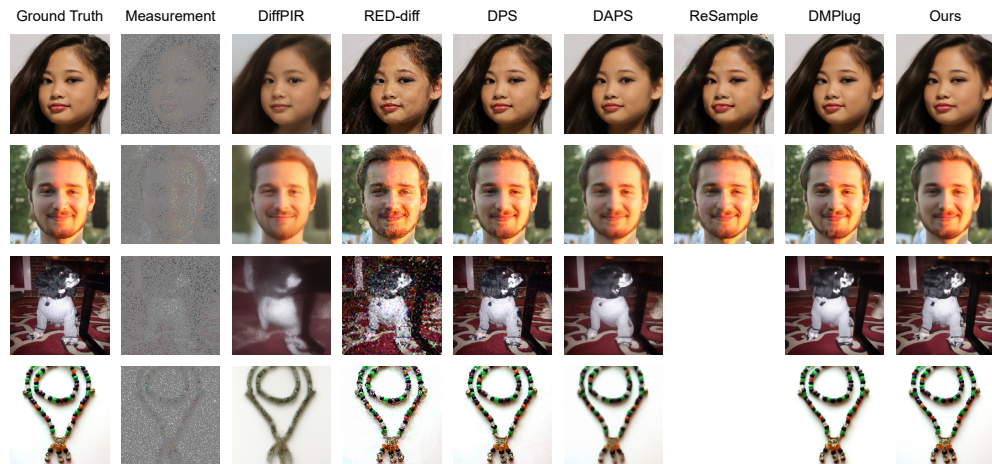


Figure 13: Random inpainting. (Top) FFHQ (256×256). (Bottom) ImageNet (256×256). $\sigma_y = 0.05$

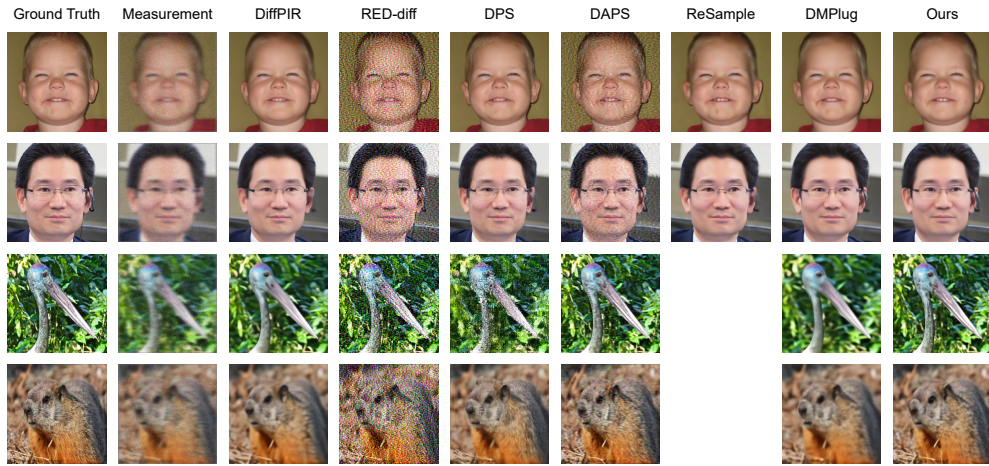


Figure 14: Gaussian deblurring. (Top) FFHQ (256×256). (Bottom) ImageNet (256×256). $\sigma_y = 0.05$

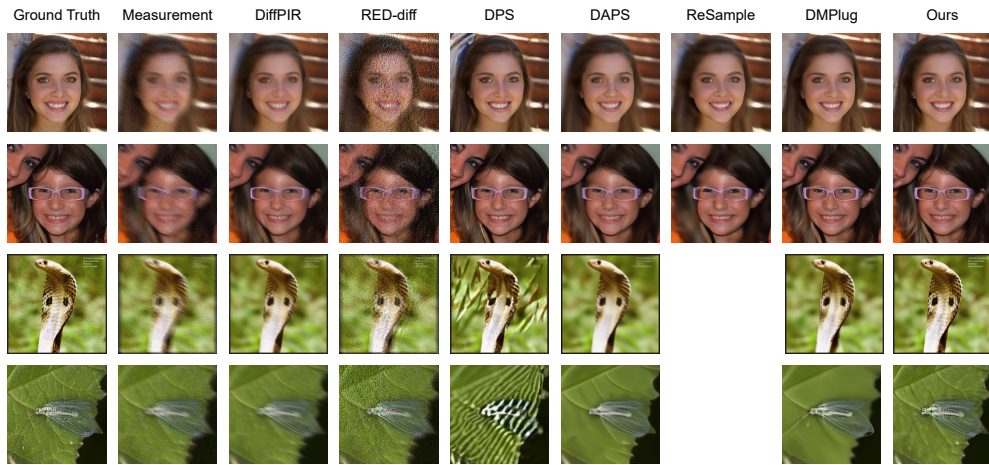


Figure 15: Nonlinear deblurring. (Top) FFHQ (256×256). (Bottom) ImageNet (256×256). $\sigma_y = 0.05$

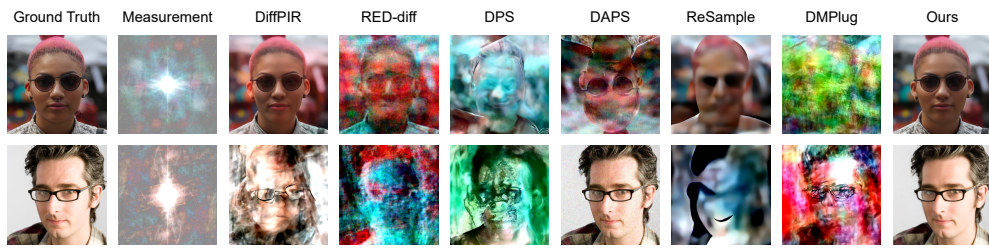


Figure 16: Phase retrieval. FFHQ (256×256).

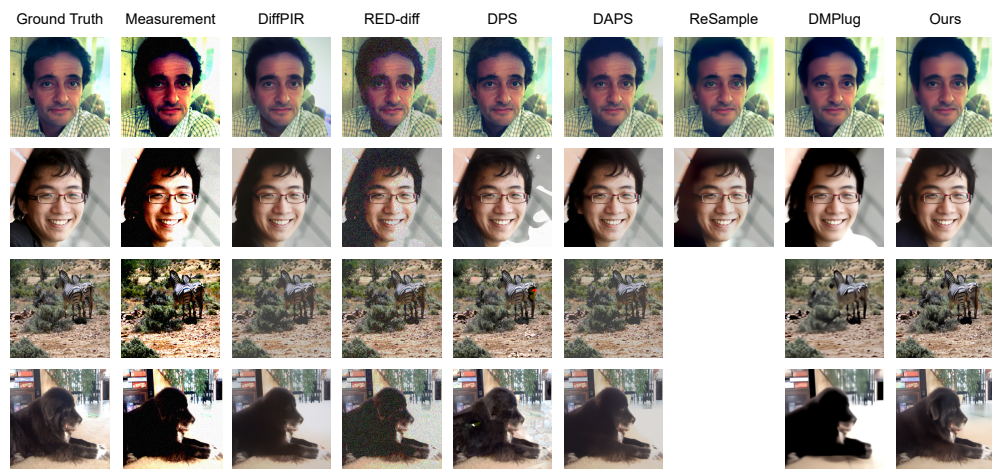


Figure 17: HDR reconstruction. (Top) FFHQ (256×256). (Bottom) ImageNet (256×256).
 $\sigma_y = 0.05$